Master's Thesis

Extended study of matter-wave diffraction from a periodic array of half-planes:
Influences of van der Waals interactions on half-plane reflection/diffraction

Ju Hyeon Lee

Department of Chemistry

Graduate School of UNIST

2019

Extended study of matter-wave diffraction from a periodic array of half-planes:
Influences of van der Waals interactions on half-plane reflection/diffraction

Ju Hyeon Lee

Department of Chemistry

Graduate School of UNIST

Extended study of matter-wave diffraction from a periodic array of half-planes:
Influences of van der Waals interactions on half-plane reflection/diffraction

A thesis/dissertation

submitted to the Graduate School of UNIST

in partial fulfillment of the

requirements for the degree of

Master of Science

Ju Hyeon Lee

07. 10. 2019

Approved by

_____

Advisor

Bum Suk Zhao

Extended study of matter-wave diffraction from a periodic array of half-planes:
Influences of van der Waals interactions on half-plane reflection/diffraction

Ju Hyeon Lee

This certifies that the thesis/dissertation of Ju Hyeon Lee is approved.

07. 10. 2019

signature

_____

Advisor: Bum Suk Zhao

signature

_____

Thomas Schultz

signature

_____

Geun Sik Lee

Abstract

Half-plane reflection/diffraction refer to overall optical phenomena occurring at a periodic array of half-planes, playing a significant role in various fields of science and technology such as statistical quantum mechanics and ultrahigh frequency communication in urban areas. In Kirchhoff approximation, these phenomena are understood as multiple scatterings over half-planes. In atom optics, such reflection mechanism was utilized to increase reflectivity of atoms from solid materials and named as "Fresnel diffraction mirror". We recently have shown that matter-wave optical phenomena from square-wave gratings are governed by edge diffraction from an array of half-planes with decreasing strip widths of square-wave gratings while quantum reflection becomes predominant as the strip widths increase. Within this thesis, we extend our previous work to study how the interaction between matter-waves and top surfaces of strips affects half-plane reflection/diffraction. Interactions between particles and surfaces, namely, van der Waals interactions, influence matter-wave diffraction from square-wave gratings in two different manners - a manifestation of quantum reflection and a reduction of reflection/diffraction efficiencies. To effectively study the latter case, i.e., an attenuation effect, we adapt a theoretical study obtained by Kouznetsov and Oberst. By comparing our measurement to the theoretical results, we find that the effects of van der Waals interactions appear differently for different particles, different grating periods and different de Broglie wavelengths. However, the adapted theoretical analysis is still not available to provide quantitative analysis for the attenuation effect. Hence, we suggest that the current theory should be improved by considering multiple scatterings of phase shifted waves induced by the van der Waals potentials in Fresnel integral. Furthermore, we look into the applicability of half-plane reflection/diffraction to van der Waals clusters and bigger molecules. Half-plane reflection of He_3 was demonstrated in our previous paper with a square wave grating, and yet it remains to be challenging to study half-plane diffraction for the van der Waals clusters due to the low diffraction efficiencies. As a breakthrough, we suggest a new type of grating which is referred to as "meta grating" by embedding a large period into a periodic array of half-planes. Such a combination of two different grating periods is expected to enable enhanced diffraction efficiencies of fragile van der Waals clusters. Besides, a theoretical study is carried out with the consideration of attenuation effects for nitrogen and helium trimer to test the possibility of applying half-plane reflection/diffraction to bigger molecules. Considering that the reflectivity goes up with decreasing grating periods, square-wave gratings of 20 μm period with 1 and 0.1 μm strip widths are used in our calculation. Compared to quantum reflection, much higher reflectivity is observed and it shows the possibility to study matter-wave optical phenomena of particles with high polarizability.

Contents

List of Figures

1   Introduction

1.1   Motivation

An electron microscope (e.g., Transmission Electron Microscope and Scanning Electron Microscope) is a powerful and irreplaceable device for various fields such as material science and biology (*1*, *2*). Electron beams with short wavelengths enable high-resolution microscopy for revealing the ultrastructure of crystals, biological and inorganic samples (*3–5*). Such an accomplishment was driven by the development of electron optical elements capable of focusing electrons into a small spot size. Matter-wave-based instruments thus has been preceded by the development of matter-wave optical elements (e.g., matter-wave mirror, beam splitter, and lens).

Motivated by the electron microscopes, a new type of matter-wave microscope has been designed with He atoms as a probe source, known as He atom microscope. By exploiting low energy (5∼100 meV) and chemical inertness of He atoms, not only insulating materials but also structures with high aspect ratio can be investigated without damaging target samples (*6*). However, the He atom microscope is limited by low intensity and resolution mainly due to a lack of proper focusing elements (*6–13*). Although atomic mirrors and zone plates have been proposed as the focusing element, limited focal spot (below 1μm) and a low transmission or reflection efficiency remain to be settled (*9–14*). Studies on atom optical elements thus are required for the realization of atom microscopes.

Among various optical elements, atomic mirrors gained increasing attention as focusing elements because they are free from chromatic aberration. Since atomic beams are not monochromatic, diffraction-based elements including lens and zone plates focus them differently depending on their velocities, causing critical defects on the microscopes. Therefore, various atomic mirrors have been actively studied with crystal metal surface, liquid helium surface, and solid materials via several reflection mechanisms as a candidate for focusing elements. Nonetheless, atomic mirrors have been impeded from an actual application on the microscopes by its low reflectivity and difficulty in controlling their curvature (*6*, *14*). As the latter case is beyond the scope of my project, the development of atomic mirrors towards high reflectivity is dealt with in this thesis.

1.2 Atom Optics

Early-stage technology was inadequate to control atomic motions while preserving their coherence due to an absence of a proper atomic source and elements. Since 1930, when Stern and Estermann observed the diffraction of He atoms from the crystal surface of lithium fluoride (*15*), subsequent studies on atom optics were halted for the next 40 years. Without an intense and coherent atomic source, neither static electric or electromagnetic field nor solid materials are suitable to change their motion, whereas both of them easily affect motions of electrons. There are two reasons for this: i) electric, magnetic and optical forces upon thermal neutral atoms are too weak to change their motion (*16*); and ii) atoms collide with rather than penetrate through the solid material, causing diffusive scattering. Therefore, the early stage of atom optics required further steps while electron optics were on a fast track (*17–22*).

A supersonic beam, developed in the 1970s, appeared to be a starting point to address the problems mentioned above (*23*). Under the supersonic expansion, atoms in a high-pressure environment, pass through an orifice into a low-pressure region. Their random thermal motions are thereby collimated, i.e., atomic wave sources with well-defined kinetic energy become available (*24*). Such supersonic beams serving as the coherent atomic source enabled various studies on the physisorption or chemisorption as well as atomic diffraction from crystal surfaces (*25–31*). The advent of supersonic beam source thus played an essential role in the revival of atom optics.

Its further progress has been accelerated by advanced technological developments in laser and nanotechnology, giving rise to the evolution of atom optical elements. There are some examples: i) enhanced coherence and intensity of the laser enabled us to observe Bragg scattering and the Kapitza-Dirac effect of atomic waves by generating a standing wave (*32–35*); ii) intense tunable laser motivated the first approach to an evanescent wave mirror (*36*, *37*) by adjusting the detuning frequency with respect to the transition frequency of atoms; iii) the establishment of nano-fabricated devices has served as atom optical elements including transmission grating (*38–40*) and Fresnel zone plate (*9*, *11*, *41*, *42*). Until now, such atom optical elements have been the basis of various instruments including matter-wave interferometry (*43–45*) and atomic de Broglie microscopy.

Driven by attempts to apply advanced laser technology to exploring atomic motion, ultracold atoms ($\sim$ nK) have been produced by laser-cooling and -trapping techniques. Such a new type of atomic source provides a high-flux and much slower atomic source. Since the de Broglie wavelength of the ultra-cold atoms is much larger than that of the thermal atoms, they accentuate the wave nature of atoms. It made a significant advance in atomic mirrors: i) normal incidence atomic reflection from the evanescent wave mirror has been attained (*46*, *47*); ii) the atomic reflection from an external magnetic field, known as magnetic mirror, has been performed for the first time (*48*, *49*) ; iii) it gave rise to the first observation of quantum mechanical

phenomena such as quantum reflection (Section 1.3.2) from a solid surface. The technological advancement is thus of paramount importance for developing atom optical elements.

1.3 Atomic Mirrors
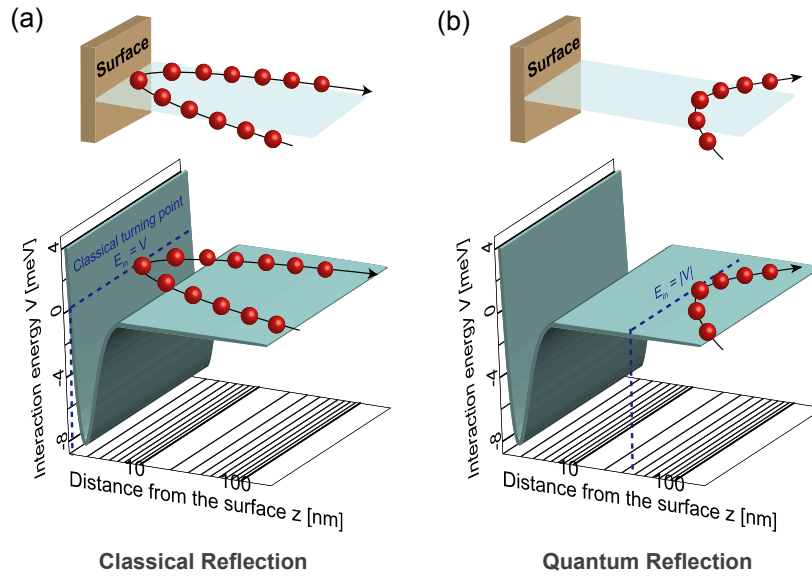
Figure 1.1: 3D representations of atom-surface collisions with corresponding potential energy surfaces induced by **a**) classical reflection and **b**) quantum reflection. (**a**) Under classical reflection, atoms collide with a surface before being reflected (top) and it occurs at the repulsive part of the potential (bottom). (**b**) [semi-classical approach] Under quantum reflection, atoms are reflected away from a surface (top) and it occurs at the attractive part of the potential (bottom).

1.3.1 Reflection Mechanism 1: Classical Reflection(CR)

In general, a reflection refers to an optical phenomenon where particles are thrown back from an object as sketched in Fig. 1.1(a). This picture is understood based on classical mechanics: classical reflection occurs at the repulsive part of the particle-surface potential where the total energy of the incident particles E_{in} equals the potential energy V as shown at the bottom of the Fig. 1.1(a). Here, the position where classical reflection takes place is called classical turning point.

Earlier studies of atomic mirrors have been performed with supersonic thermal beams via He atom scattering (HAS) from crystal surfaces at near normal incidence. Under typical experimental conditions for HAS, classical reflection most likely occurs at the surface (*31*). In other words, when atoms are classically reflected from the surface, the atomic reflection happens close to outmost atoms on the surface so they are influenced by the local variation of the potential along the surface, i.e., surface roughness and adsorbates on the surfaces cause incoherent reflection. Complicated surface-preparation processes (e.g., annealing and sputtering) and ultra-high vacuum ($\sim 10^{-12}$ mbar) are therefore crucial to render surfaces smooth at the atomic-level and to prevent surfaces from being affected by surroundings during the whole experiment, respectively (*25–30*). However, even a perfectly clean surface may have unexpected surface defects (i.e., surface steps, adatoms, and vacancies), decreasing reflectivity (*50, 51*).

Thus, the efficiency of classical reflection from crystal surfaces has been limited by its high sensitivity to the surface quality (*52–54*).

For the reasons as mentioned earlier, atomic mirrors was initially studied in a way that atoms are prevented from colliding with surfaces. As examples, an evanescent wave mirror and a magnetic mirror use evanescent waves and magnetic fields respectively to prevent atom-surface collisions. The artificial repulsive potentials induced by those fields push atoms away from the surface before they reach the surface so that reflectivity of both mirrors can be tentatively 100 %. However, both mirrors have difficulty in making large in size without compromising accuracy. Because magnetic mirrors are constructed by a delicate fabrication process like lithography techniques (*49*) and the evanescent wave is attenuated as propagating along the surface, causing diffusive scattering (*55*). Thus, even with a remedy to minimize the reduction of reflectivity caused by the atom-surface collision, atomic mirrors using external fields have been limited by technical limitations.

1.3.2 Reflection Mechanism 2: Quantum Reflection (QR)

From the point of view of classical mechanics, particles are likely to be stuck onto a surface rather than reflected when their incident kinetic energies become zero. This phenomenon, referred to as sticking, has been studied to understand gas-surface interactions as well as surface catalytic reactions (*56–59*). On the other hand, it has been found that the sticking is suppressed when atoms are reflected at long-range interactions before being accelerated towards the repulsive potentials (*60*). Such a non-classical mechanism is called quantum reflection. There are two different perspectives on the origin of the quantum reflection: semi-classical approach and quantum mechanical approach.

As an extension of studies on the sticking process, quantum reflection has been generally understood as a breakdown of WKB approximation (semi-classical approach) while a different aspect of quantum reflection was recently suggested based on a pure quantum mechanical calculation by Miret-Artés and Pollak (pure quantum mechanical approach) (*61*). Although basic principles are different for each representation, both have indicated that quantum reflection occurs away from a classical turning point as the energy of incident atoms is decreased. An experimental observation of reflection of fragile helium dimers from a solid material has given clear evidence for that (*62*). Hence, when particles are quantum mechanically reflected from objects, an atomic scale irregularity on the surface hardly affects the reflectivity, i.e., surface-preparation processes are not required.

Semi-classical approach (local effect)

Quantum reflection has been known to occur when the WKB approximation breaks down where a local variation of a de Broglie wavelength is rapid. To quantify how rapidly the de

Broglie wavelength changes in space, badlands function $B(z)$ is introduced as below:

$$B(z) = \hbar^2 \left(\frac{3}{4} \frac{(p')^2}{p^4} - \frac{1}{2} \frac{p''}{p^3} \right),$$ (1.1)

where p is the momentum of a particle and z is the distance between atoms and a surface. For the WKB approximation to be valid, the badlands function should be significantly zero. Theoretical studies based on this aspect have revealed that quantum reflection takes place where the incident energy of atoms E_{in} equals the absolute value of the potential $|V|$ as depicted in Fig. 1.1(b) (*60*, *63*). In addition, it has been found that fluctuations of the spatial de Broglie wavelength occur at several hundreds or thousands of atomic unit away from the surface (*64*). In such a condition, particles are under the influence of solely an attractive part of the atom-surface interaction, known as Casimir-van der Waals potential. In other words, a repulsive part of the potential has nothing to do with quantum reflection. The approximated form of Casimir-van der Waals potential is given by the equation below:

$$V(z) = -\frac{C_3 l}{(z+l)z^3},$$ (1.2)

C_3 is the van der Waals coefficient which describes the strength of the interaction and l is a characteristic length related to the transition wavelength between the electronic ground state and the first excited state of an atom or a molecule. In the semi-classical representation, quantum reflection is considered to be a local effect which occurs only at around the badlands region.

Pure quantum mechanical approach (non-local effect)

Miret-Artés and Pollak have recently proposed that quantum reflection is a coherent non-local interference process between overall scatterings occurring from the whole part of the interaction potential, refuting the semi-classical representation. In 2016, they carried out a theoretical analysis for experimental results on quantum reflection of He atoms from solid materials by considering a repulsive part of the potential as well as an attractive part of the potential. In that paper, they concluded that quantum reflection has a non-local property and not related to the long-range badlands region of the potential (*61*). Furthermore, their group have provided a numerical analysis to solve the time-dependent Schrödinger equation on quantum reflection with a Morse potential and an Eckart potential in a subsequent paper. By comparing their results to the semi-classical studies, they reiterated that quantum reflection has nothing to do with the badlands function, but it is a consequence of the non-local characteristic of scatterings (*65*).

Thus far, most of the theoretical studies on quantum reflection have been performed through the semi-classical representation. The reasons for this is that the analytical formula is readily obtained in the semi-classical regime and the pure quantum mechanical approach has only

recently been suggested. Therefore, theoretical calculations for quantum reflection have been done by adapting the semi-classical approach in our project (Section 2.1 for further information).

To experimentally investigate quantum reflection from solid materials, the particle's kinetic energies perpendicular to the surface must be sufficiently small. There are two ways to achieve this prerequisite: i) using ultra-cold atoms to exploit their small kinetic energies; ii) employing a grazing incidence condition.

Ultra-cold metastable neon atoms, produced by laser-trapping technique, led to the first observation of quantum reflection of atoms from a solid material (*66*). Driven by such pioneering research, numerous studies on quantum reflection from the attractive part of the atom-surface interaction have been carried out with various solid materials like silicon or glass surface and even with structured surfaces both theoretically and experimentally (*67–71*). As a result of those active studies, solid materials are finally found to be one of atomic mirrors whose reflectivity can reach 100 % as the vertical energy of atoms $E_z \to 0$. Here, it is noteworthy that bare solid materials without any applied field have been finally revealed as a decent atomic mirror through quantum reflection.

Instead of generating ultra-cold atoms, grazing incidence conditions have been used to study quantum reflection of thermal atoms from solid materials (*72, 73*). In typical experimental conditions, the grazing incidence angle of a few mrads provides a sufficiently small vertical kinetic energy, perpendicular to the surface. Hence, when incident matter-waves propagate almost parallel to the surface of a mirror or a grating, even fast atoms can be coherently reflected from the surface. Furthermore, such a small incidence angle enables us to observe diffraction of matter-waves from micro-fabricated gratings as well as nano-fabricated gratings: distinct resolved diffraction peaks have been observed from micro-fabricated reflection-gratings, demonstrating the coherent nature of the quantum reflection (*74–76*). It is notable that micro-fabricated gratings can take the place of nano-fabricated gratings in terms of an available tool to observe matter-wave diffractions (Appendix A). The grazing incidence condition thus plays a significant role in studying quantum reflection of thermal atoms.

1.3.3   Reflection Mechanism 3: Half-plane Reflection/Diffraction (HF)

A periodic array of half-planes, an infinite number of parallel semi-infinite planes periodically placed, has functioned as a simple model for the theoretical study of wave scatterings from systematically structured surfaces. When a plane wave propagates along an array of half-planes at a grazing incidence angle of θ_{in}, some parts of it are blocked by the half-planes (see Fig. 1.2). According to the uncertainty principle, blocking waves reduce uncertainty of propagating waves in coordinate space, giving rise to increased uncertainty in momentum space. The blocking waves thus cause diffraction at each of the half-planes. As long as such near field diffraction is strong enough to influence subsequent units of half-planes, a multiple scat-
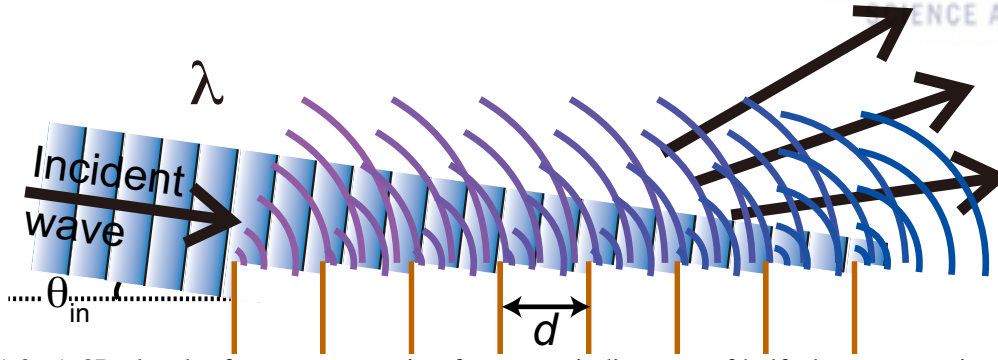
Figure 1.2: A 2D sketch of a wave-scattering from a periodic array of half-planes at grazing incidence angle θ_{in}. A wavelength of incident waves and a period of parallel half-planes are denoted by λ and d, respectively.

tering takes place over the edges of the half-planes and it features overall optical phenomena occurring at the periodic array of half-planes. In addition, the periodical property of this system induces certain conditions under which the constructive interference of diffracted waves at each half-plane is generated, resulting in distinct diffracted waves as well as reflected waves. These optical phenomena are referred to henceforth as "half-plane reflection/diffraction".

Various theoretical studies of the half-plane reflection/diffraction have been carried out for electromagnetic waves. The exact solution of the boundary value problem for the reflection of electromagnetic waves was obtained by Carlson and Heins using the Wiener-Hopf integral equations (77, 78). Developed formulae capable of dealing with diffraction as well as reflection were derived in subsequent theoretical studies (79, 80). In 2003, Bogomolny and Schmit found an asymptotic behavior of multiple scatterings which is described by a single parameter u, figured below (81):

$$u = \sqrt{\frac{2d}{\lambda}} \sin\frac{\theta_{in}}{2}, \tag{1.3}$$

where d is the period of parallel half-planes and λ is the wavelength of a wave, thus extending the Carlson and Heins' work to the semi-classical limit of the small wavelength at grazing incidence conditions. It is noteworthy that it can describe the same optical phenomena of different wave sources which are in different ranges of wavelengths. Until now, such theoretical descriptions have applied to various fields of science and technology including optics (82), statistical quantum mechanics (83–85), and ultra-frequency (0.1–1 m) communication (86–88) to explain reflection and diffraction of waves occurring at periodic structures.

However, only recently has it been validated that such theoretical model is applicable for atomic waves (69). Experimental observations of the half-plane reflection/diffraction in atom optics have started with attempts to deal with a difficulty of quantum reflection from solid materials (70, 71): even with ultra-cold atoms, a quantum reflection probability from a flat surface decreases rapidly as the atoms' kinetic energy perpendicular to the surface becomes large, i.e.,

(a)

(b)
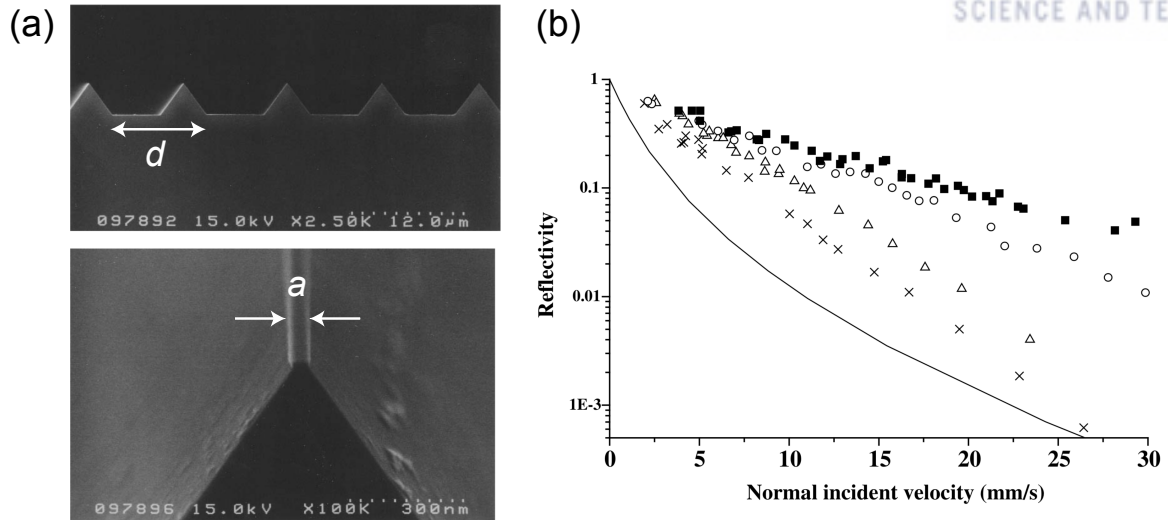
Figure 1.3: (**a**) A cross-sectional view (top) and an expanded view (bottom) of scanning microscope images of the silicon grating surface. Definition of a period d and a width a of the ridge are depicted. (**b**) Reflectivity of atoms from various ridged surfaces are plotted as a function of the normal incident velocity of the atoms. A solid line show the reflectivity from the flat surface. Both **a**) and **b**) are extracted from (*71*)

the flat solid surface is no longer a proper atom reflector at larger incidence angles. To prevent such a drastic reduction of the reflectivity at larger incidence angle, periodically structured surfaces have been utilized as a supplementary tool by decreasing the effective density near the surface, namely giving smaller C_3 values in Eq. (1.2). Such analysis based on quantum reflection provided a qualitative picture of the experimental results, and yet it was insufficient to give a quantitative interpretation.

To our knowledge, the first investigation of quantum reflection from a periodically structured surface has been reported by Shimizu and Fujita in 2002 (*71*). They performed an experiment using several ridged silicon surfaces that have a period d between 10 and 100 μm and a width a of the ridge between 40 nm and 11 μm. Images of one of the used ridged surfaces are shown in Fig. 1.3(a) with definitions of the period d and the strip width a. Fig. 1.3(a) and 1.3(b) are Figure 1 and Figure 3 from reference (*71*), respectively. As shown in Fig. 1.3(b), the overall reflectivity of ridged silicon surfaces (symbolic scatters) is much higher than that of the flat silicon surface (solid line). Furthermore, weak first-order diffraction was observed from the ridged surface that has 1 μm-wide ridges and a period of 100 μm.

Motivated by the above-mentioned experimental work, theoretical works have been undertaken to understand the origin of the optical phenomena from regularly structured surfaces. Shimizu and his coworkers have given quantitative analysis in two separate papers (*69, 70*): two of the authors, Kouznetsov and Oberst, developed a detailed description in the latter paper (*69*). In order to simplify calculations, the array of ridges was assumed to be an array of ideal half-planes, i.e., the strip width a is assumed to be infinitesimally small. Based upon a per-

9

spective of the wave-scattering induced by Fresnel diffraction at each edge of the ridges, they found that the atomic reflection from grating structures depends mainly on a single parameter

$$\beta = \sqrt{\frac{2d}{\lambda}}\theta_{\text{in}}. \tag{1.4}$$

Kouznetsov and Oberst introduced a different parameter p by adding a pre-factor to β such that $\sqrt{\pi}\beta$ in their latter paper (*69*). Here, it is noteworthy that the both parameters are proportional to the single parameter u (Eq. (1.3)) such that $\beta = 2u$ and $p = 2\sqrt{\pi}u$. As shown in Fig. 1.4(a), experimentally obtained reflectivity from various silicon surfaces (symbolic scatters) as a function of the single-parameter β converges to the same curve while exponentially decaying in β. Note that this single parameter is completely independent of both atomic species and surface materials.
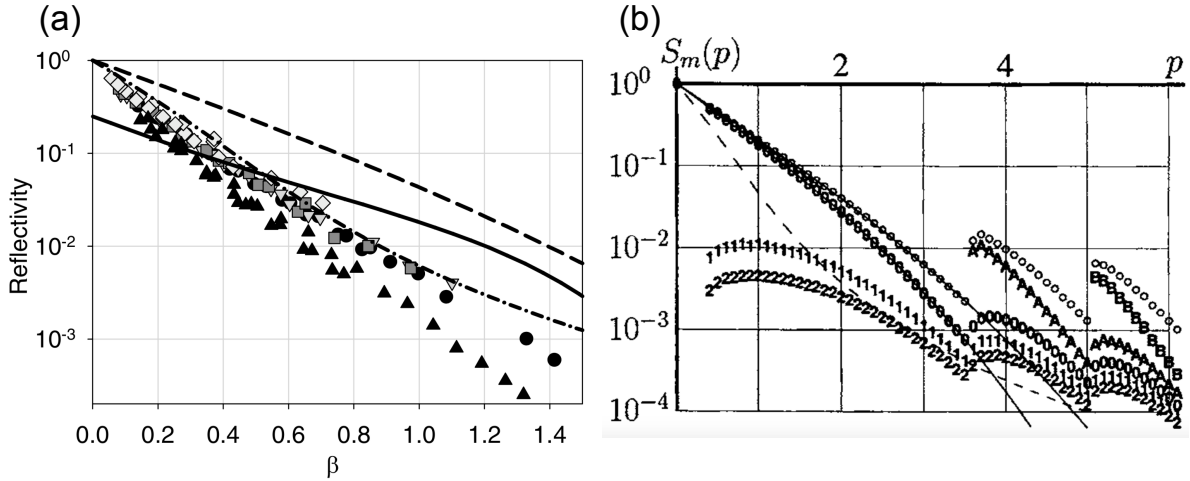
Figure 1.4: (**a**) The reflectivity of metastable neon and helium from the same ridged grating surface which period is 5 μm and strip width is 100 nm as a function of the parameter β. A solid line is the reflectivity calculated by Fresnel integral (*70*). A dashed line (dash-dotted line) is the numerically calculated result (*69*) (the empirical result obtained by assuming an equivalent medium with effective absorption rate $\frac{\nu}{d}$ (*69*)). (**b**) The reflection and diffraction efficiencies S_m as a function of the parameter p ($= \sqrt{\pi}\beta$) up to the 2nd diffraction order. Digits and circles show the numerical results of m-th order diffraction efficiencies and total efficiency of scattering summing up to the 8th order, respectively. The empirical result is denoted by a dashed line (same line in (**a**)). Both figures are taken from (*70*) and (*69*).

Initially, they assumed that Fresnel diffraction is not strong enough to cause multiple scatterings. It gave rise to a useful description above, and yet theoretical result under this assumption (solid line) was inadequate to explain diffractions and to reproduce the experimental data (symbolic scatters) as shown in Fig. 1.4(a) (*70*). In the latter paper (*69*), the multiple scattering was included in the calculation so that Fresnel diffraction occurring at a half-plane was considered to influence the overall wave-scattering at the next units of half-planes. Here, not only specular but also diffraction efficiency up to the 2nd order were calculated both numerically (see Fig.
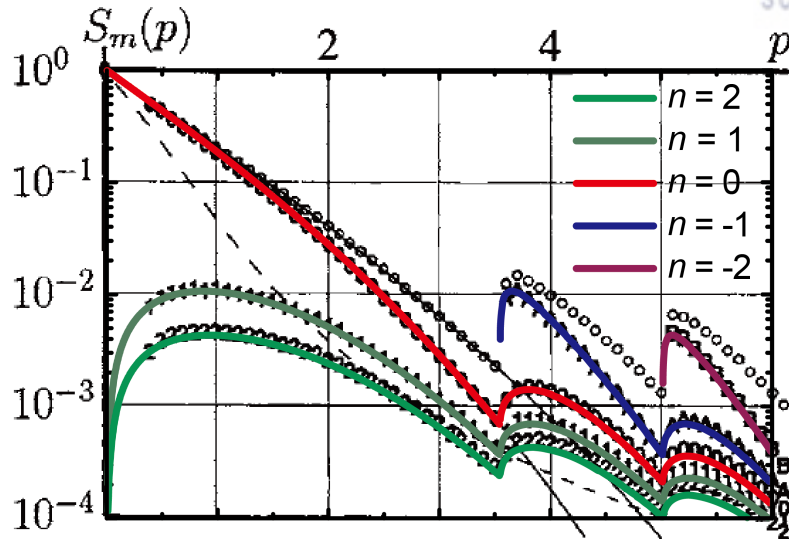
Figure 1.5: The same image of Fig 1.4(b) is taken here to compare with the theoretical result calculated by Bogomolny and Schmit as marked with colored lines (*69*, *81*). A notation for the diffraction order is n in this paper, whereas m is used for the diffraction order in Ref (*69*).
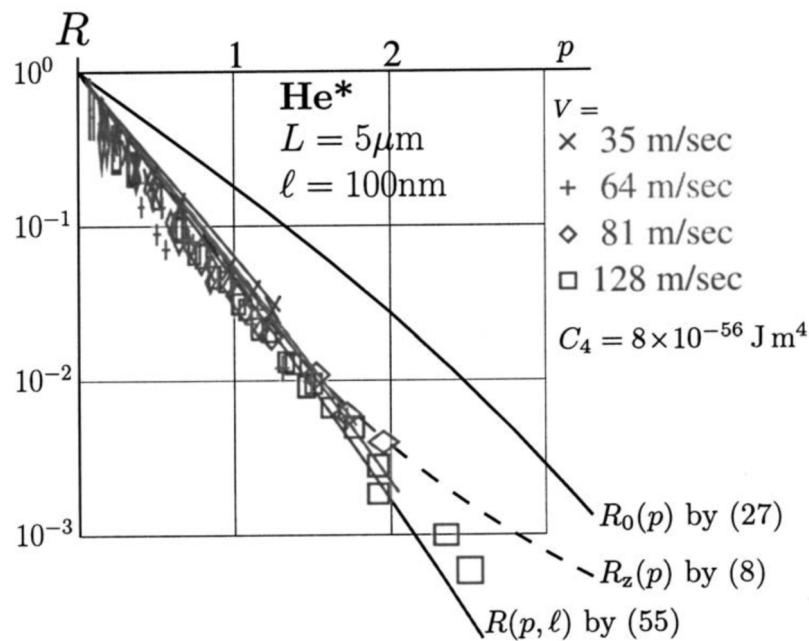
Figure 1.6: This image is taken from (*69*). Here, a period d and a strip width a are denoted with different letters L and l, respectively. A solid line denoted by $R_0(p)$ shows the numerical result of specular efficiency. A dashed line of $R_z(p)$ describes the empirical result. They are the same lines with the solid and the dashed-dotted lines presented in Fig. 1.4(a), respectively. $R(p, l)$ shows the corrected result by considering van der Waals interactions.

1.4(b)) and analytically. It is remarkable that their numerically calculated results are identical to the theoretical results of the analytical formula obtained by Bogomolny and Schmit (Section 2.2 for details) as shown in Fig. 1.5 (*81*). It implies that half-plane reflection/diffraction are key

11

to atom optical phenomena from periodically structured surfaces. It has a significant meaning for developing a new type of atomic mirrors in the sense that the reflectivity can be higher than quantum reflection mirror by adjusting the period of the array of half-planes.

Even with the consideration of multiple scatterings, theoretical results were still not able to describe the experimental results (dashed line in Fig. 1.4(a)). Regarding this disagreement, the authors pointed out that the interaction between atoms and surfaces might reduce the reflectivity (*69*). In order to estimate the effect of the interaction quantitatively, an additional phase shift induced by the atom-surface interaction over the finite strip width of the ridges was introduced (Section 2.2.2 for further information). By calculating the distance where waves are out of phase due to the potential, the reduction of the reflectivity was calculated. As shown in Fig. 1.6, the corrected data $R(p, l)$ denoted by a solid line, shows better agreement with the experimental results. Thus, that atom-surface interactions over the finite strip width a should still be considered for matter-wave half-plan reflection/diffraction.

1.4   Summary of Work Presented in This Thesis

In our previous work, we observed fully resolved matter-wave diffractions up to the 2nd order from the square-wave grating of 400 μm period and strip width ranging from 10 to 200 μm at grazing incidence conditions (*89*). We found that the diffraction of He atoms from the grating with 10 μm strip width mainly results from half-plane reflection/diffraction, while quantum reflection becomes more prominent as strip widths increase. In addition, half-plane reflection/diffraction of matter-waves were experimentally investigated in a wide range of u from 0.5 to 2 by exploiting thermal particles under grazing incidence conditions. Diffraction efficiencies as well as specular efficiencies are observed, thereby a comprehensive experimental verification for the theoretical analysis of half-plane reflection/diffraction produced by Bogomolny and Schmit (*81*) (later, Kouznetsov and Oberst reported the same theoretical results in the separate paper (*69*)) was performed.

In this thesis, we extend our previous work to study the ways in which the interaction between matter-waves and the a top-surface of a finite width affects half-plane reflection/diffraction. The particle-surface interaction, i.e., the van der Waals interaction, influences the matter-wave diffractions from the square-wave gratings in two different manners – quantum reflection and an attenuation effect. Firstly, in order to better understand an interplay between quantum reflection and half-plane reflection/diffraction, one of our previous results (*89*) is reproduced along with corresponding results for D_2. We observe that each particle exhibits different propensities of diffraction efficiencies, suggesting different influences of quantum reflection. On the other hand, as strips become narrow, the effect of the van der Waals interaction reveals as a reduced probability of half-plane reflection/diffraction rather than a manifestation of quantum reflection. Regarding this, Kouznetsov and Oberst pointed out earlier that the van der Waals interaction near a strip of the gratings induces an additional phase shift along the path of matter-waves, and, therefore, reduces the reflectivity (*69*). They theoretically analyzed such an attenuated probability of half-plane reflection/diffraction for specular reflection ($n = 0$). To effectively study such effects in our experimental condition, where not only reflection but also diffraction is observed, we extend their theoretical analysis to the diffraction efficiencies as well. The interaction effects are thereby investigated for different particles of He and D_2, different grating periods, and different de Broglie wavelengths.

Meanwhile, the reflection of fragile He_3 from a square wave grating via half-plane reflection/diffraction was experimentally demonstrated within our previous work and it raises the question as to whether it is possible to apply such a half-plane model system to molecules generally. To look into the possibility, we reproduce the previous result of the reflectivity of He trimers from a square-wave grating of 400 μm period and 10 μm strip width. Considering that specular probability of half-plane reflection/diffraction can be increased by decreasing the scalable parameter u, i.e., by reducing the period of the half-planes, we carry out a theoretical

analysis for reflectivities of nitrogen and helium trimer (de Broglie wavelengths of each one are 37.0 and 106 pm) from square-wave gratings of a 20 μm period and narrow strip widths (less than 1 μm). Even with the consideration of the particle-surface interaction, specular efficiencies for both particles are sufficiently high to be measured at incidence angles ranging from 0.5 to 2 mrad, opening up the possibility for a new type of general atomic/molecular mirror.

2 Theoretical Calculation

In the real world, it is inevitable for strips of square-wave gratings have a finite width. Therefore, quantum reflection as well as an edge diffraction from an array of half-plane occurs above the square-wave gratings by the interaction between atoms/molecules and the strips. For a quantitative analysis, the numerical calculations for both quantum reflection and half-plane reflection/diffraction are carried out and presented in this section. Furthermore, a reduction of the reflectivity at the narrow strip width (less than 10 μm) is discussed in terms of the atom-surface interaction for different particles, different periods of square-wave gratings, and different de Broglie wavelengths.

2.1 Quantum Reflection
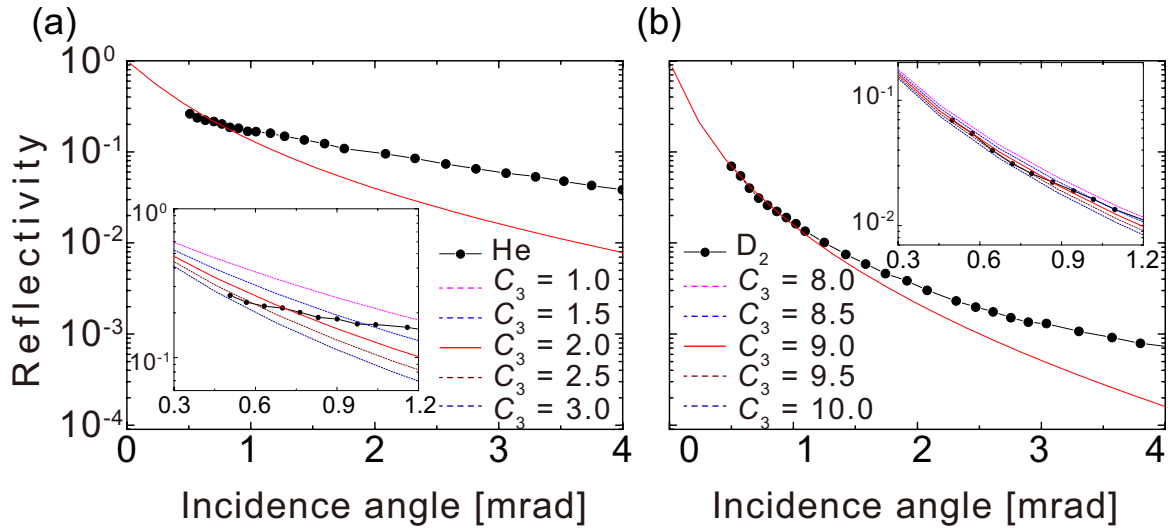
Figure 2.1: Reflectivity from the blank photoresist for (**a**) He atoms and (**b**) D_2 molecules at source temperature of 51.8 K. The experimental reflectivities and the best fits are depicted with full black circles and red solid lines, respectively. The unit of the van-der Waals coefficient C_3, 10^{-50} Jm^3 is omitted in the legends for the sake of visibility. The insets in each graph show theoretical lines calculated for 5 different values of C_3 along with experimental results in the range of 0.3 to 1.2 mrad of incidence angle which are considered in fitting process.

We adopt the semi-classical approach whereby quantum reflection is explained as a local effect. In order to estimate the effect of quantum reflection on our experiment, theoretical and experimental reflection probabilities of a flat surface of photoresist, the same material with the square-wave grating used in our experiment (Appendix C), are obtained. For theoretical analysis, we solve 1D Schrödinger equation numerically including the Casimir-van der Waals potential for each value of the van der Waals coefficient C_3 (see Eq. (1.2)). Here, characteristic lengths l for He and D_2 are 9.25 nm and 17.3 nm, respectively. The van der Waals coefficient is determined by fitting the calculated quantum reflection probability to the experimental result

15

of the blank photoresist surface. Figure 2.1 shows the reflectivity of the flat surface of photoresist and best fits of theory line calculated for each particle. The C_3 value for the best fit is determined through the method of least squares in a logarithmic scale as below:

$$\sum_{i=1}^{num} (log(exp_i) - log(thoery_i))^2, \qquad (2.1)$$

ith experimental value and corresponding theoretical value are denoted by exp_i and $theory_i$, respectively. As the reflection from the repulsive part of the potential has been known to be more prominent at larger incidence angles (*72, 73*), only first 10 data points and 9 data points in the range of 0.3 to 1.2 mrad of the incidence angle are taken into account to the sum of the squared residuals for He and D_2, respectively.

He		D_2	
C_3 [10^{-50}Jm^3]	$\sum$(residuals)^2	C_3 [10^{-50}Jm^3]	$\sum$(residuals)^2
1.0	1.52	8.0	0.17
2.5	0.38	8.5	0.05
2.0	0.36	9.0	0.02
2.5	0.94	9.5	0.07
3.0	1.87	10.0	0.20

Table 2.1: Sum of squared residuals at each C_3

5 different C_3 values with the corresponding sums of the squared residuals for He and D_2 are listed in Table 2.1. Experimental data points which are taking part in the fitting procedure along with fitting curves for each C_3 value are shown enlarged in insets of Fig. 2.1. As the least square values are determined at $C_3 = 2.0 \times 10^{-50}$ Jm^3 and $C_3 = 9.0 \times 10^{-50}$ Jm^3 for each source, the best fits are found with those values.

2.2 Half-Plane Reflection/Diffraction

2.2.1 Edge Diffraction from a Periodic Array of Half-Planes
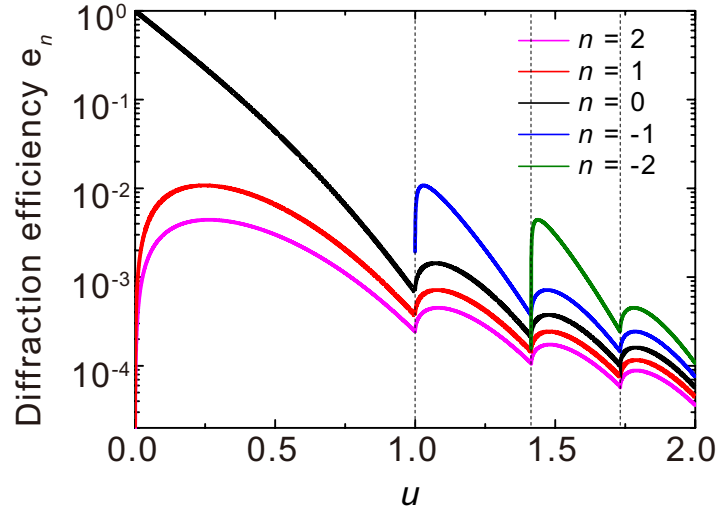
Figure 2.2: This image is taken from (*89*). Diffraction efficiencies $e_n(u)$ for the specular ($n = 0$) and for diffracted beams up to the second order calculated by adapting the Bogomolny-Schmit solution given by Eqs. (2.2) and (2.3).

In 2003, Bogomolny and Schmit extended the preceding theory done by Carlson and Heins (*77*, *78*) to the semiclassical limit of the small wavelength at grazing incidence conditions by finding the asymptotic behavior of multiple scatterings (*81*), i.e., their work is appropriate to analyze our experimental results. The same results were obtained 2 years later by Kouznetsov and Oberst (*69*) as a separate work to understand matter-wave optical phenomena from the ridged surfaces. Here, we borrow the theoretical work of Bogomolny and Schmit to investigate our experimental results. Analytical formulae of reflection coefficients, derived in their paper (Eq. (98) in Ref. (*81*)), is multiplied with the factor $\frac{u_n}{u} \sim \frac{\sin\theta_n}{\sin\theta_{\text{in}}}$ due to the fact that the flux of scattered particles is the main concern in our experiment so diffraction efficiencies e_n are described as below:

$$e_n = \frac{4uu_n}{(u + u_n)^2} G(u)G(u_n), \tag{2.2}$$

where n is a diffraction order, and

$$G(x) = e^{2x\zeta(\frac{1}{2})} \prod_{l \geq 1} e^{\frac{-2x}{\sqrt{l}}} \prod_{\substack{l > 0 \\ l \neq [x^2]}} \left| \frac{1 + (x/\sqrt{l + \{u^2\}})}{1 - (x/\sqrt{l + \{u^2\}})} \right|. \tag{2.3}$$

Here, $[x]$ and $\{x\}$ are the integer and the fractional part of the x such that $x = [x] + \{x\}$, the constant $\zeta\left(\frac{1}{2}\right) = -1.460354$ is given by the Riemann zeta function, and $u_n = \sqrt{n + u^2} = \sin(\theta_n/2)\sqrt{2d/\lambda}$. Thus, e_n not only depends on θ_{in} but also on the n th-order diffraction

17

order to estimate an infinite product in Eq. (2.3), we set the value of the upper limit for the
product $l_{\max}$ to 80000. We regard this value as a fairly large number because the difference
between e_n calculated with $l_{\max} = 60000$ and 80000 is less than 1%. Figure 2.2 shows the
numerically calculated efficiencies as a function of the single parameter u.

Distinct minima of each curve and perfect reflectivity at $u = 0$ feature in the half-plane
reflection/diffraction:

1. When the new mth order diffraction beam emerges from a periodically structured sur-
   face, clear minima appear in reflection and diffraction efficiencies. It may be linked
   to emerging beam resonance (*75*) (in general, EBR stands out as an abrupt intensity
   change of the diffraction efficiencies), corresponding to Rayleigh-Wood anomalies in
   photon diffraction. In such a condition, the incidence angle is defined as Rayleigh angle
   denoted by $\theta_{R,m}$ such that $\cos\theta_{R,m} - 1 = \frac{m\lambda}{d}$. By putting this to Eq. 1.3, the following
   relation is derived, $u_{R,m} = \sqrt{m}$.

2. The reflection efficiency e_0 approaches 1, while diffraction efficiencies e_n drop to 0 in
   the limit $u \to 0$. While a reflectivity of quantum reflection can be increased by adjusting
   a de Broglie wavelength or a grazing incidence angle, a reflectivity from a periodic array
   of half-planes can be increased by controlling the period of the structures as well. It
   implies that half-plane reflection/diffraction can provide a promising approach for the
   atomic mirror.

2.2.2 Attenuation Factor (AF)

Kouznetsov and Oberst explained the mismatch between the experimental results and the
theoretical results of the edge diffraction from an array of parallel half-planes (see Fig. 1.4(a))
as considering the interaction between atoms and the finite width of the ridge in their previous
paper (*69*). The dispersive interactions, i.e., Casimir-van der Waals interaction, in the vicinity
of the strips have been attributed to a reduction of the reflectivity. To effectively study the
influence of matter-wave interactions, the attenuation factor is introduced in this section by
adopting the previous analysis done by Kouznetsov and Oberst (*69*).

They firstly estimated a phase shift induced by the atom-surface interaction. The additional
phase shift destroys the phase synchronization over the surface and leads to out-of-phase waves
with respect to the original reflected waves. To decide the portion of the reflected waves under
the influence of the potential, two characteristic distances s and s_0 corresponding to out-of-
phase waves and a main contribution of the Kirchhoff integral were evaluated:

1. the marginal distance s where the additional phase shift becomes larger than 1 rad is de-
   rived within the regime of Casimir-van der Waals potential (Eq. 1.2), which corresponds

to our experiment condition, is figured as below:

$$s^3 = (\frac{(a + 2s)C_3 l}{\hbar v(s + l)}),$$ (2.4)

where v is the velocity of atoms.

2. characteristic distance s_0 is described as below:

$$s_0 = \frac{1}{k\theta_{\text{in}}},$$ (2.5)

k is the momentum of the atoms.

Here, s is determined by numerically calculating the formula of Eq. (2.4) with a 10^{-16} step size of s. Such an iterative procedure is repeated until the difference between LHS (left-hand side) and RHS (right-hand side) is less than 10^{-28}. The intensity of the attenuated waves $R(u, a)$ therefore can be approximated by the following relation:

$$R(u, a) = \exp(-\frac{s}{s_0})e_0,$$ (2.6)

e_0 is the theoretical result of the specular efficiency ($n = 0$) formulated by Eq (2.2). As an explicit function of the single parameter u, Eq. (2.6) can also be represented as below:

$$R(u, a) = (-\sqrt{\frac{8}{d\lambda}}\pi u s)e_0.$$ (2.7)

Additionally, for the efficiencies of non-zero nth order diffractions, we tentatively define the attenuated intensities of diffracted waves by substituting θ_{in} by $\frac{(\theta_{in} + \theta_n)}{2}$:

$$R(u_n, a) = \exp(-\sqrt{\frac{2}{d\lambda}}\pi (u_n + u)s)e_n.$$ (2.8)

Thus, $R(u_n, a)$ depends on both u and u_n.

An attenuation factor for specular efficiency is defined as an exponential term $\exp\left(-\frac{s}{s_0}\right)$ in Eq. (2.6). Figure 2.3 shows the attenuation factors as a function of u to study the different effects of particle-surface interactions on half-plane reflection/diffraction for different particles and strip widths, periods of sqare-wave gratings, and de Broglie wavelengths,

The attenuation effects are stronger for D_2 than He and for larger strip widths as shown in Fig. 2.3(a). In general, particles with larger polarizability, namely larger C_3 values, interact more strongly with surfaces so the attenuation factor decreases more rapidly for D_2 than that for He at the same square-wave grating while a stronger additional phase shift emerges upon top-surfaces of wider strips, causing more severe reduction of the reflectivity. When both the

19
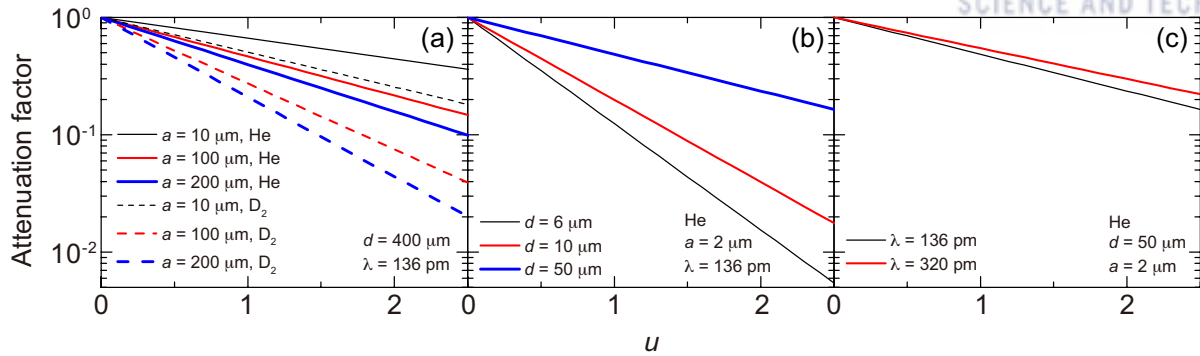
Figure 2.3: Attenuation factors as a function of a scalable parameter u at different conditions: **a**) at fixed period and wavelength, **b**) fixed strip width and wavelength, **c**) fixed period and strip width. (**a**) A black solid line (black dashed line) represents the attenuation factor from the grating with strip width of 10 μm for He (D_2) while a red solid line (red dashed line) and a blue solid line (blue dashed line) describe those from the gratings with strip width of 100 μm and strip width of 200 μm for He (D_2), respectively. (**b**) Attenuation factors for the period of 6 μm, period of 10 μm and period of 50 μm are described by a black solid line, a red solid line and a blue solid line, respectively. (**c**) A black solid line (red solid line) shows the attenuation factor for the wavelength of 136 pm (wavelength of 320 pm)

strip width and the de Broglie wavelength are fixed, overall additional phase shifts upon the top surface of the strips are the same. However, when it is presented as a function of the scalable parameter u, attenuation factors are presented differently for different periods of the gratings. In other words, the correspondence between scalable parameter u and the period of gratings makes different effects as shown in Fig. 2.3(b). When it comes to the different wavelengths, however, the problem is not as simple as it seems because both marginal distance s and the original contribution to the Kirchhoff integrals s_0 are dependent on the wavelength. They are affected reversely by the change of the wavelengths. Therefore, even though the difference of marginal distances is relatively large, attenuation factors are not so much different from each other as shown in Fig. 2.3(c).

3 Instrument and Method

3.1 Grazing Incidence Atom Optics Apparatus (MAGIE)
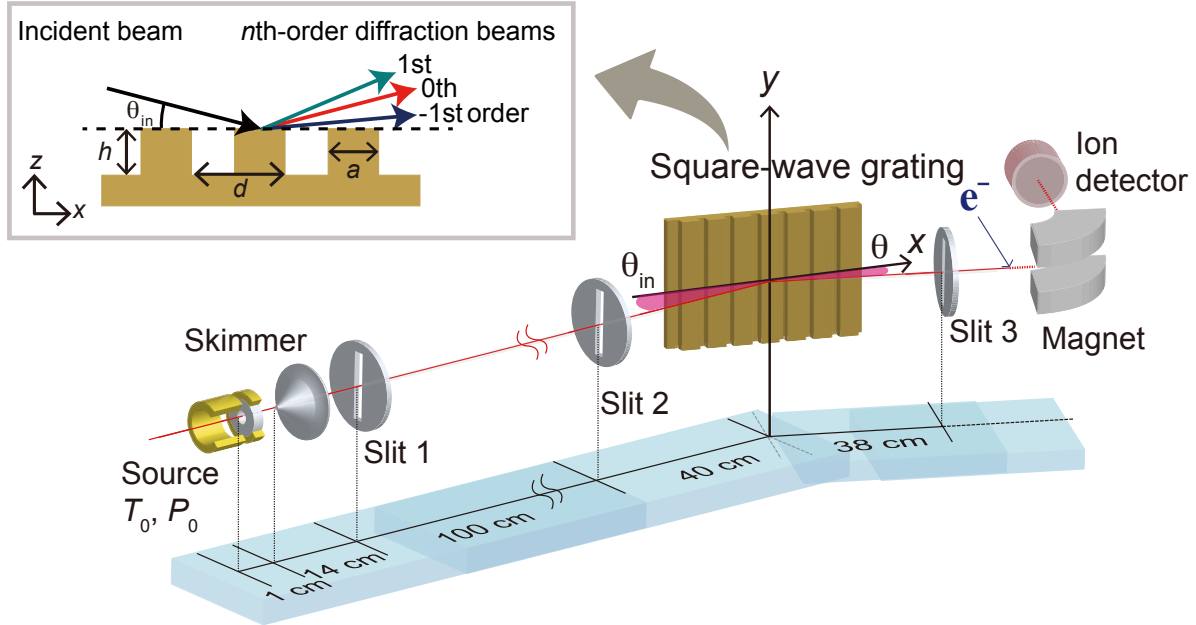
Figure 3.1: Schematic of the experimental apparatus for the experimental observation of the matter-wave reflection or diffraction. The inset box depicts the wave-scattering from a square-wave grating with a period d and a strip width a as well as the definition of a sign of the diffraction order n. The height of the structures on the substrate is denoted by h. The coordinate system is indicated in the figure.

A high-angular-resolution grazing incidence atom optics apparatus has been utilized for previous studies on matter-wave diffractions or reflections under grazing incidence condition (*62, 73–76*). A schematic of the apparatus is depicted in Fig. 3.1. Either continuous, cold He or D_2 beam is formed by supersonic expansion of each source through 5 μm of the orifice at stagnation pressure P_0 and source temperature T_0. Liquid helium is used to cool down the source.

	T_0	P_0	ν	λ_{dB}
He	51.8 K	26 bar	760 m/s	136 pm
	9.40 K	0.5 bar	300 m/s	320 pm
D_2	51.8 K	2.0 bar	760 m/s	136 pm

Table 3.1: Source conditions

Table 3.1 shows the used source temperatures and stagnation pressures along with corresponding velocities and de Broglie wavelengths of each source. Here, the temperature and the pressure are set for the cluster formation of each beam to be restricted so that negligible fraction of clusters are expected in our measurement (*90*). The continuous beam is collimated by the slit 1 and collimated once again by the slit 2 (slit width: 20-μm) after passing through a

21

skimmer and two differential pumping chambers (see Fig. 3.1). Here, the width (height) of the both slits is 20-μm (1 mm height) and they are 1 m apart from each other. The collimated beam is scattered from the square-wave grating with period d and strip width a. The periods and strip widths together with the height of the structures of square-wave gratings which we conducted our experiment with are described in Fig. 3.2. In addition to the gratings, a flat surface (not structured) coated with photoresist is prepared to examine the effect of reflection from the flat-top surface on the half-plane reflection/diffraction.
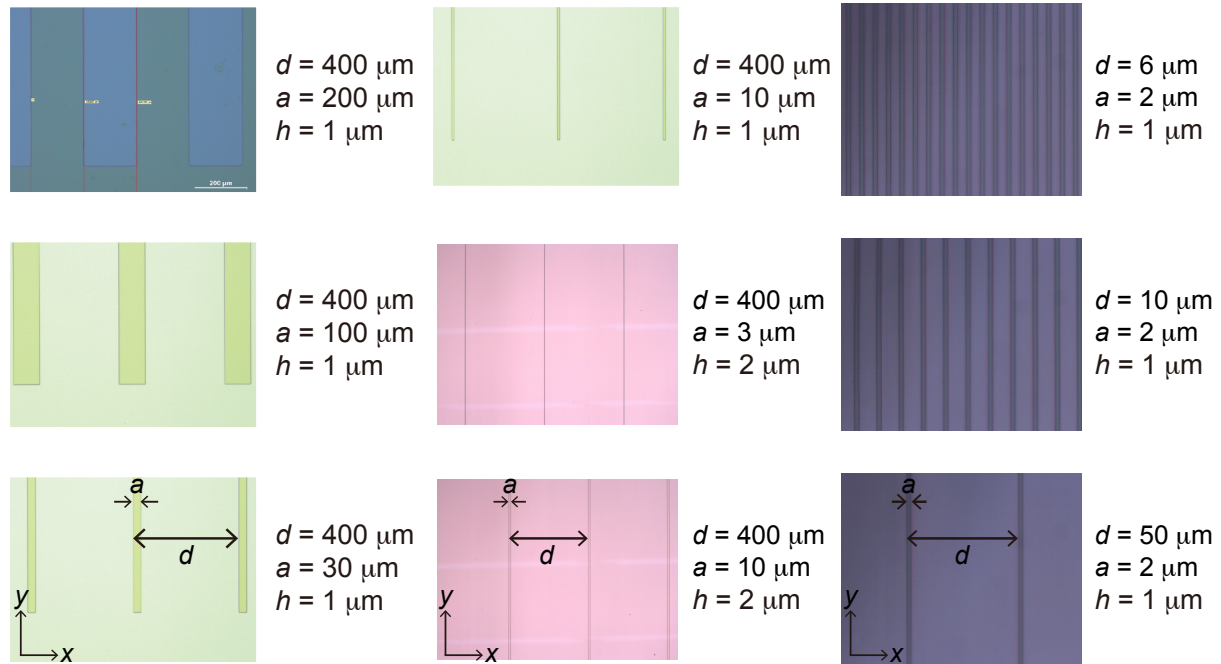
Figure 3.2: Microscope images of 9 different square-wave gratings used in this work.

Here, the grating is mounted for a pivotal movement about y-axis so that we can control the incidence angle θ_{in} and grating normal is set to be z-axis. Before arriving at the detector, the scattered beam passes through the 25-μm-width-slit 3 (5 mm height), 48 cm further downstream from the grating. The combination of three slits gives rise to a high angular resolution of 110 μrad (full width of half maximum of direct beam, see Fig. 3.3(c)) in our experiment. The whole detecting part including slit 3, electron impact ionizer, and mass-spectrometer is precisely rotating to measure ion signals of the scattered beam. Here, the grating pivotal axis is very close to the detector pivotal axis so that we assume that they share the axis.

3.2 Angular Spectrum
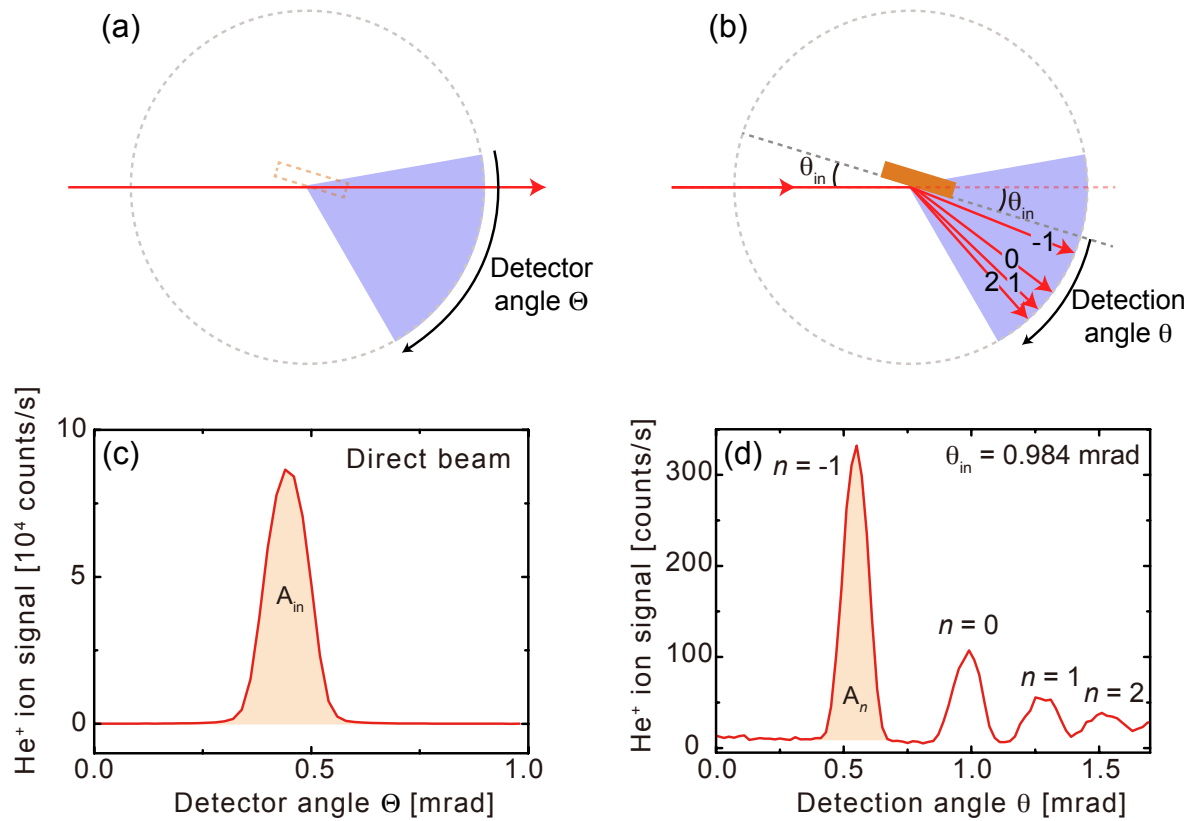
Figure 3.3: Geometrical descriptions (not to scale) for a detection method (**a**) when a grating is removed from the beam path to measure the direct beam and (**b**) when grating is mounted within the beam path to lead to matter-wave scatterings. Red arrows and purple-shaded regions show the beam path and detection regime covered by rotating mass-spectrometer, respectively. (**c**) An angular distribution of direct He beam as a function of the detector angle Θ measured at $T_0 = 51.8$ K and $P_0 = 26$ bar. (**d**) The He atomic beams scattered from the square wave grating with a 400-μm period and a 10-μm strip width are measured as a function of detection angle θ at incidence angle θ_{in} of 0.984 mrad. The reflection ($n = 0$) and the diffraction peaks ($n \neq 0$) appear when the grating is located within the beam path as shown in **b**).

In our experiment, angular spectra are measured by the precisely rotating detector. Fig. 3.3(a) and 3.3(b) show schematic descriptions of our detection approach along with definitions of a detector angle and a detection angle. The detector angle is measured with respect to one end of the rotating detector while the detection angle is defined from the plane of $z = 0$ including the grating surface. Although initial angular spectra (see Fig. 3.3(c)) are measured as a function of the detector angle, they are more likely to be presented as a function of the detection angle (see Fig. 3.3(d)) so that center positions of each peak directly indicate a reflection or diffraction angles. In order to investigate efficiencies of reflection and diffraction on our experiment, not only scattered beams but also incident beams should be considered. While the scattered beam is simply measured when the grating is mounted inside the beam path, a further correction

(Section 3.3) is necessary to obtain the incident beam. Although an original incident beam, named as "direct beam" in our work, is easily measured when the grating is removed from the beam path as depicted in Fig 3.3(c), the direct beam can be cut or blocked by the grating under the grazing incidence condition, giving rise to a reduction of the incident beam.

3.2.1 Determination of Parameters

Incidence angle θ_{in}, diffraction angle θ_n, and n-th order diffraction efficiency e_n (0th order diffraction efficiency is the specular efficiency) are important parameters in our experiment. To determine such parameters, we perform a Gaussian fit to each peak in the angular spectrum. The fitting parameters are the center position, the width, and the height of a peak. As a result of the fitting procedure, the width w_n, the area A_n and the center position x_n are derived in terms of the detector angle. The definitions of each parameter are given by following relations,

$$\theta_{\text{in}} = (x_{direct} - x_0)/2, \tag{3.1a}$$

$$\theta_n = x_n - x_{direct} - \theta_{in}, \tag{3.1b}$$

$$e_n = A_n/A_{incident}. \tag{3.1c}$$

The fitting error introduces an uncertainty of about 1 μrad to 5 μrad in the angle determination depending on whether there is overlap with neighboring peaks or not. The diffraction peaks have a full width at half-maximum (FWHM) of about 110 μm.

3.3   Awing Analysis

(a)

Direct beam profile

wing profile

wing

Blocked
direct beam

Scattered
beam

(b)

50 mm

θ_{in}

6 mm

$(50 \times \theta_{in})$ mm

50 μm
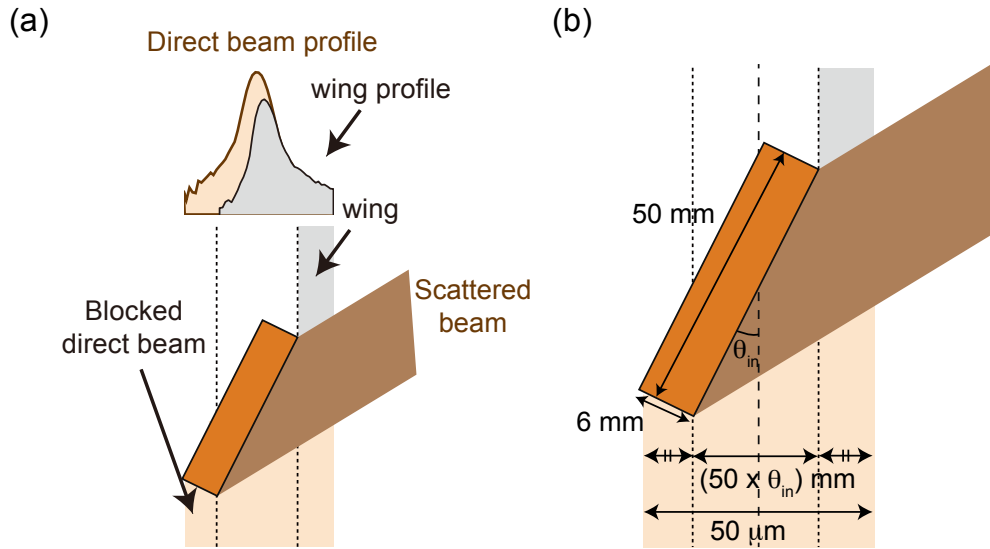
Figure 3.4: (**a**) Description of a direct beam (apricot) and a partial loss of that (grey) under the grazing incidence condition (not to scale). The half of the loss can be measured and is named as "wing". (**b**) A close-up of **a**) without profiles. Measurements of the gold mirror used in our work and beam diameter are denoted.

The square-wave gratings used in this work are photoresist-patterned on a commercial square gold mirror (Thorlabs PFSQ20-03-M03) which face diameter is 50 mm and thickness is 6 mm (the details about fabrications are in Appendix C). Figure 3.4 shows the sketch of the direct beam-loss occurring at the grazing incidence condition as well as the actual measurement of each component. As indicated in Fig. 3.3(b), when the gold mirror is mounted, the direct beam is partially clipped or blocked at grazing incidence angles less than 1 mrad. As the cut or blocked direct beam does not affect the actual scattering process, it should be ruled out of the incident beam. However, there is no way to obtain the blocked beam directly, while the cut direct beam, called "wing" in this thesis, is easily measured. In order to estimate such a blocked beam indirectly, the mirror should be positioned for the surface of the mirror to be centered so that the amounts of the wing and the blocked direct beam are the same as shown in Fig. 3.3(b) (see Appendix B for details). The gaussian peak area of the incident beam A_{incident} is thereby defined as the difference between those areas of the direct beam and the wing, $A_{\text{direct}} - 2A_{\text{wing}}$.

3.4 Formation of Helium Trimer

Conditions for cluster formations in a supersonic expansion of ^{4}He atoms have been studied with nano-transmission gratings (*90*), and therefore optimum source conditions - temperature $T_0 = 8$ K and pressure $P_0 = 2$ bar are set to obtain most probable mole fraction for helium trimers in our experiment. Nonetheless, it might be almost impossible to set trimers apart from other clusters including monomers for a specular peak at the 4 amu He-ion mass. Therefore, mass spectrometer was set at mass 8 amu to circumvent such an issue whereby measured signals are considered to stem from the scatterings of helium trimers, not monomers nor dimers.

4 Results and Discussion

4.1 Interplay between Half-Plane Reflection/Diffraction and Quantum Reflection

To study the different effects of quantum reflection induced by the interaction between atoms/molecules and a top surface of the strips on half-plane reflection/diffraction for different particles, one of our previous results is reproduced in Fig. 4.1 (first column) (*89*) along with corresponding results for D_2 (second column). Different propensities for matter-wave diffractions of He and D_2 for n from -2 to 2 using various square-wave gratings of fixed period $d = 400\,\mu$m with different strip widths $a = 10,\ 30,\ 100,\ 200\,\mu$m are thereby presented. In addition to diffraction efficiencies from each square-wave grating, reflectivities of each source from a blank photoresist surface (without any structures on it) are measured and marked with black full circles at the third row in Fig. 4.1. For a qualitative comparison between two different reflection mechanisms - quantum reflection and half-plane reflection/diffraction, theoretical results (see Section 2) are plotted by red dashed and red solid lines, respectively.

For both particles, diffraction efficiencies e$_n$ for relatively narrow strip widths are more likely to follow the theory lines of half-plane reflection/diffraction (HP theory line) - not only efficiencies but also distinct minima exhibit clear features of half-plane reflection/diffraction. On the other hand, they tend towards the theory line of quantum reflection (QR theory line) with increasing strip widths – specular efficiencies (non-specular efficiencies) become larger (eventually approach Fraunhofer-Kirchhoff constants) and minima are diminishing especially at larger Rayleigh angles $\theta_{\mathrm{R},m}$ (i.e., $u = \sqrt{m}$). In other words, optical phenomena from the gratings with shorter strip widths are governed by half-plane reflection/diffraction while quantum reflection takes it over as the strip widths become larger. Optical phenomena of matter-waves from the square-wave gratings thus result from the interplay between HP and QR.

However, the details are quite different for He and D_2. Compared to He, there are three characteristic differences on results of D_2: i) measured efficiencies with $a = 30\,\mu$m are in good agreement with the HP theory lines at $\theta_{\mathrm{in}} < 1.17$ mrad while overall efficiencies with the same grating are much higher than the HF theory lines for He; ii) minima of diffraction efficiencies at Rayleigh angles $\theta_{\mathrm{R},m}$ are weak even for $a = 10\,\mu$m as the incidence angle is increased while the corresponding results for He exhibit clear minima even for the wider strips, i.e., $a = 30\,\mu$m; iii) overall observed efficiencies are below the HP theory lines for $a = 10\,\mu$m while those are slightly higher than HP theory lines for He, especially for $n = 0$ and 1.
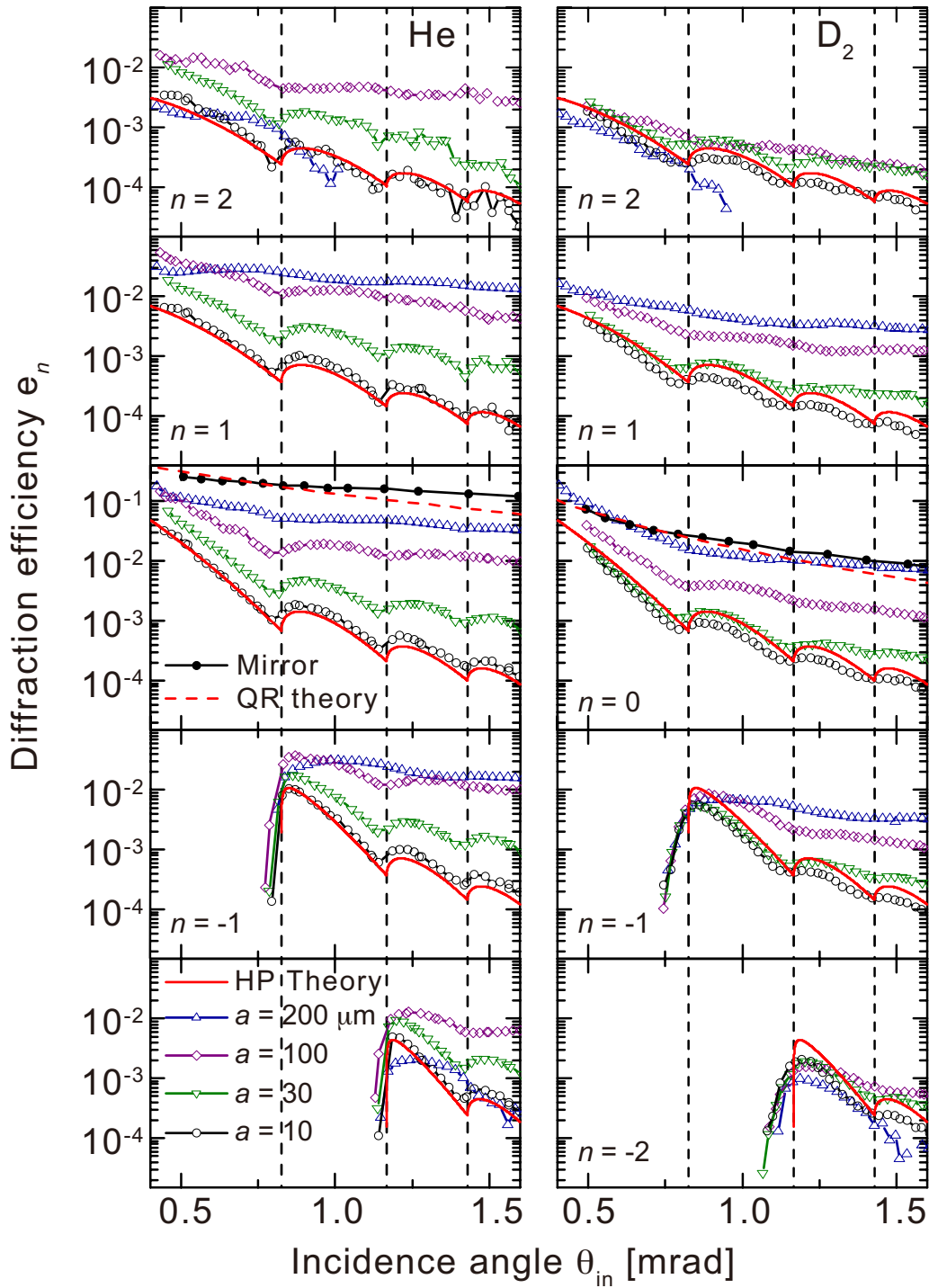
Figure 4.1: Diffraction efficiencies e_n of He (left column) and D_2 (right column) from square wave gratings of period $d = 400\ \mu$m with strip widths $a = 10, 30, 100, 200\ \mu$m at source temperature of 51.8 K (corresponding de Broglie wavelength $\lambda = 136$ pm) on a logarithmic scale. Red solid lines show the theoretical result calculated for edge diffractions from an array of half-planes (Eq. (2.2)). The graphs on the third row (for the cases of $n = 0$) also include the measured reflectivities of He (left column) and D_2 (right column) from the flat surface of photoresist (full black circles) as well as best fitting-curves of quantum reflection (red dashed line).

One of the big differences between the two particles is polarizability – D_2 has about 3.9 times larger polarizability than He. The particles with larger polarizability interact more strongly with surfaces, giving rise to lower quantum reflection probability and more vigorous attenuation effects. All the features mentioned above are therefore understood as the simultaneous effects of diminishing quantum reflection and stronger attenuation effects for D_2: reduced quantum reflection accentuate half-plane reflection/diffraction even for the strip width $a = 30\ \mu$m, while stronger attenuation effects result in weaker minima as the strip widths and incidence angle increase. Meanwhile, regarding the weaker minima, broader velocity spread of D_2 has been known to be one of the reasons as well (*91*), yet it is not enough to explain the gradually diminishing minima with the increasing incidence angles.

In general, for wider strips, attenuation factors are decreased more rapidly (see Fig. 2.3(a)), while quantum reflection increases proportionally to the width of a flat-top-surface (*89*). Our analysis described here shows a general tendency, explicating the interplay between quantum reflection and half-plane reflection/diffraction plays a major role on matter wave diffractions from the square wave gratings. However, it only gives us a qualitative picture, and therefore, studies on sole effects for each case are required for quantitative analysis. Although the sole influence of quantum reflection can be indirectly studied by applying Fraunhofer-Kirchhoff diffraction theory under the assumption that the reflectivity from the flat-top surfaces of the gratings is estimated by the reflectivity of the flat surface multiplied by the ratio *a/d,* similar studies on the attenuation effect still have difficulties as the theoretical analysis on attenuation factor remains to be verified in a wider range of u.

Finding a suitable condition under which quantum reflection can be suppressed is therefore essential to exclusively study the attenuation effect. However, it is still ambiguous to determine where to draw a line of such condition, i.e., it is a question of how narrow the strip width has to be to exclude quantum reflection. Here, the results of D_2 for the square-wave grating of the 10 μm strip width are noticeable in a sense that the overall efficiencies are even below the HP theory lines. It implies that quantum reflection hardly takes place over the top surface of the strips at this condition. Motivated by this observation, we perform a subsequent analysis with narrower square-wave gratings as presented in the next section.

4.2 Attenuation Effects on half-plane reflection/diffraction

4.2.1 Different Particles

To deal with the above-mentioned issue, a similar investigation is implemented for the strip widths of 3 μm and 10 μm. Figure 4.2 shows diffraction efficiencies of He and D_2 from square-wave gratings of 400 μm period with 3 μm (left column) and 10 μm (right column) strip widths along with the theory lines of attenuated efficiencies, calculated by multiplying HP theory lines by attenuation factors. The gratings used here are newly produced to control other variables such as surface contamination which may affect diffraction efficiencies. Although the height of the structures are 2 μm rather than 1 μm (the height of the strips for all the gratings used in Section 4.1 is controlled to be 1 μm), overall results obtained with new grating of strip width 10 μm are similar with the observation measured from the corresponding grating prepared in the past (see Fig. 4.3).

For the grating with 3 μm-wide strips, both particles exhibit diffraction efficiencies lower than the HP theory lines while only D_2 exhibits lower efficiencies than the HP theory lines for 10 μm-wide strips. Furthermore, the experimental results from the 10 μm strip width are higher than those from the 3 μm strip width for each particle. In fact, the resultant efficiencies for the 10 μm strip width are supposed to be lower than those for the 3 μm strip width in theory, yet the experimental results show the opposite tendency. Additionally, we find that the theoretically obtained attenuated efficiencies, marked with dashed black lines (dotted black lines) for He (D_2), are always lower than the experimental results for the 10 μm strip width. Such a disagreement between the experimental results and the theoretical results indicates that quantum reflection remains to affect the matter-wave reflection/diffraction from the grating for the 10 μm strip width, limiting the isolated study of the attenuation effect.

Hence, we have focused on the results obtained with the grating of strip width 3 μm to effectively study the attenuation effect, and thereby see the availability of the theoretical model for the attenuation effect. According to the theoretical description of the attenuation factor (Section 2.2.2), the attenuation effect is considered to be more prominent as u increases, yet the experimental results for He are rather closer to the HP theory lines with increasing u. It suggests that we can not completely ignore the effect of quantum reflection even at the narrower strip width for the case of He. Even so, we find that the theoretically obtained attenuated efficiencies for both particles are in fairly good agreement with the experimental results as long as u is smaller than the corresponding value of the first Rayleigh angle $\theta_{R,1}$ ($\theta_{R,|n|+1}$ for $n < 0$). After the certain value of u, the theory lines of attenuated efficiencies increasingly deviate from the observed efficiencies as u increases and it is not clear whether such a disagreement results from the manifestation of quantum reflection or the limitation on the theory of attenuation effect.

Despite all the factors mentioned above, the theoretical model for the attenuation effects provides the qualitative information – stronger particle-surface interactions for D_2 cause more

prominent attenuation effects than He, and, therefore, D_2 exhibits lower diffraction efficiencies. In addition, diffraction efficiencies which are even below the HP lines imply that we should account for the particle-surface interactions to understand matter-wave optical phenomena from the square wave gratings, namely periodically structured surfaces. Therefore, the current theoretical model for the attenuation effect should be improved to address those optical phenomena quantitatively. As a first step for this, we investigate matter-wave optical phenomena for different conditions in following sections – different grating periods (Section 4.2.2) and de Broglie wavelengths (Section 4.2.3) to look into the limiting factors for the current theory. Now that we know that quantum reflection can hinder the attenuation effect, the strip widths of the gratings are fixed at 2 μm which is the narrowest width that the conventional photolithography technique can produce (Appendix C).
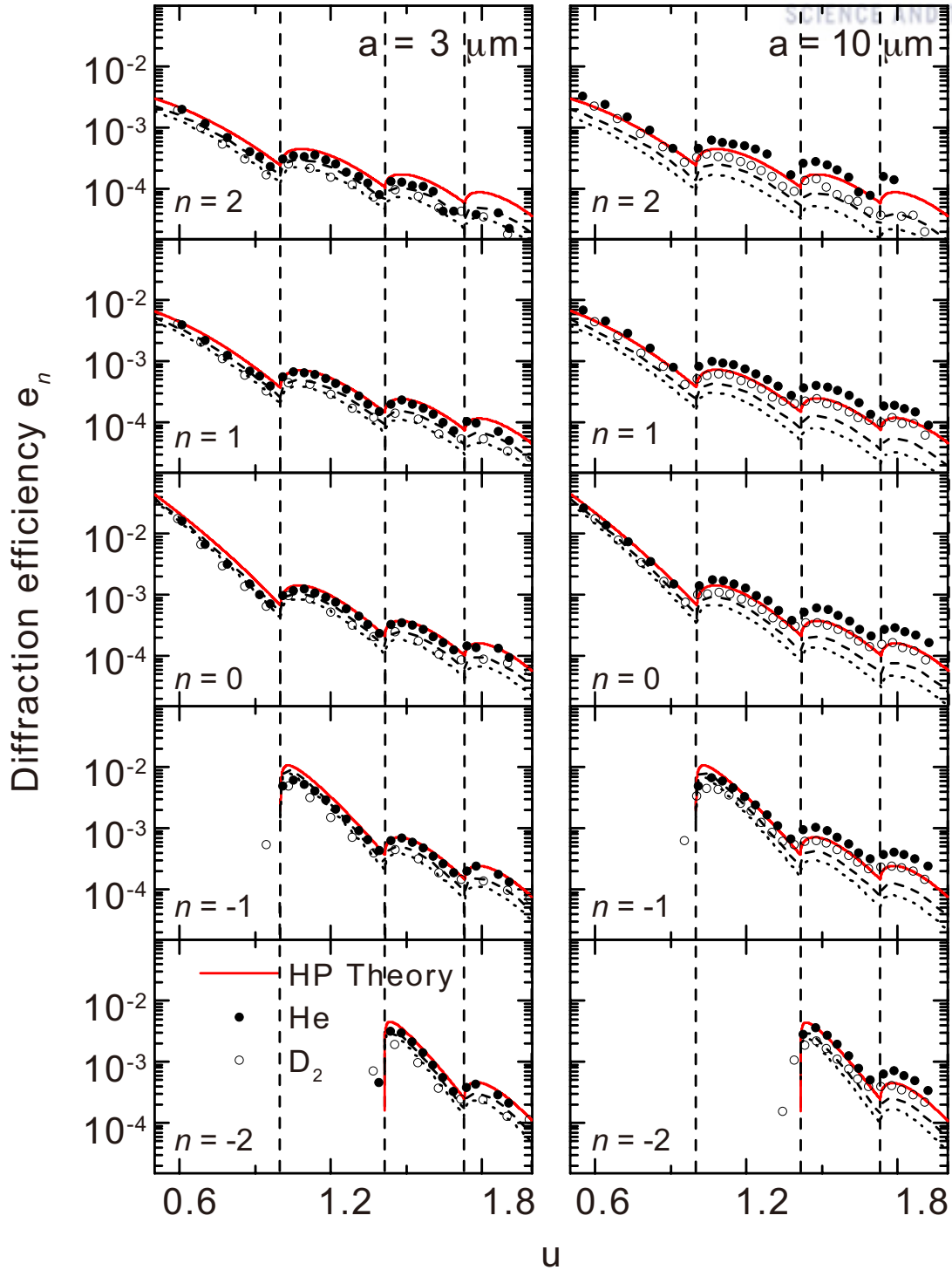
Figure 4.2: Diffraction efficiencies e_n of He (full black circles) and D_2 (open black circles) as a function of u measured from square wave gratings of period $d = 400$ μm with strip widths $a = 3$ μm (left column) and 10 μm (right column) at source temperature of 51.8 K (corresponding de Broglie wavelength $\lambda = 136$ pm) on a logarithmic scale. Red solid lines show the theoretical result calculated for an array of half-planes. Theoretical calculations for attenuated efficiencies for He and D_2 are marked with black dashed and black dotted lines, respectively.
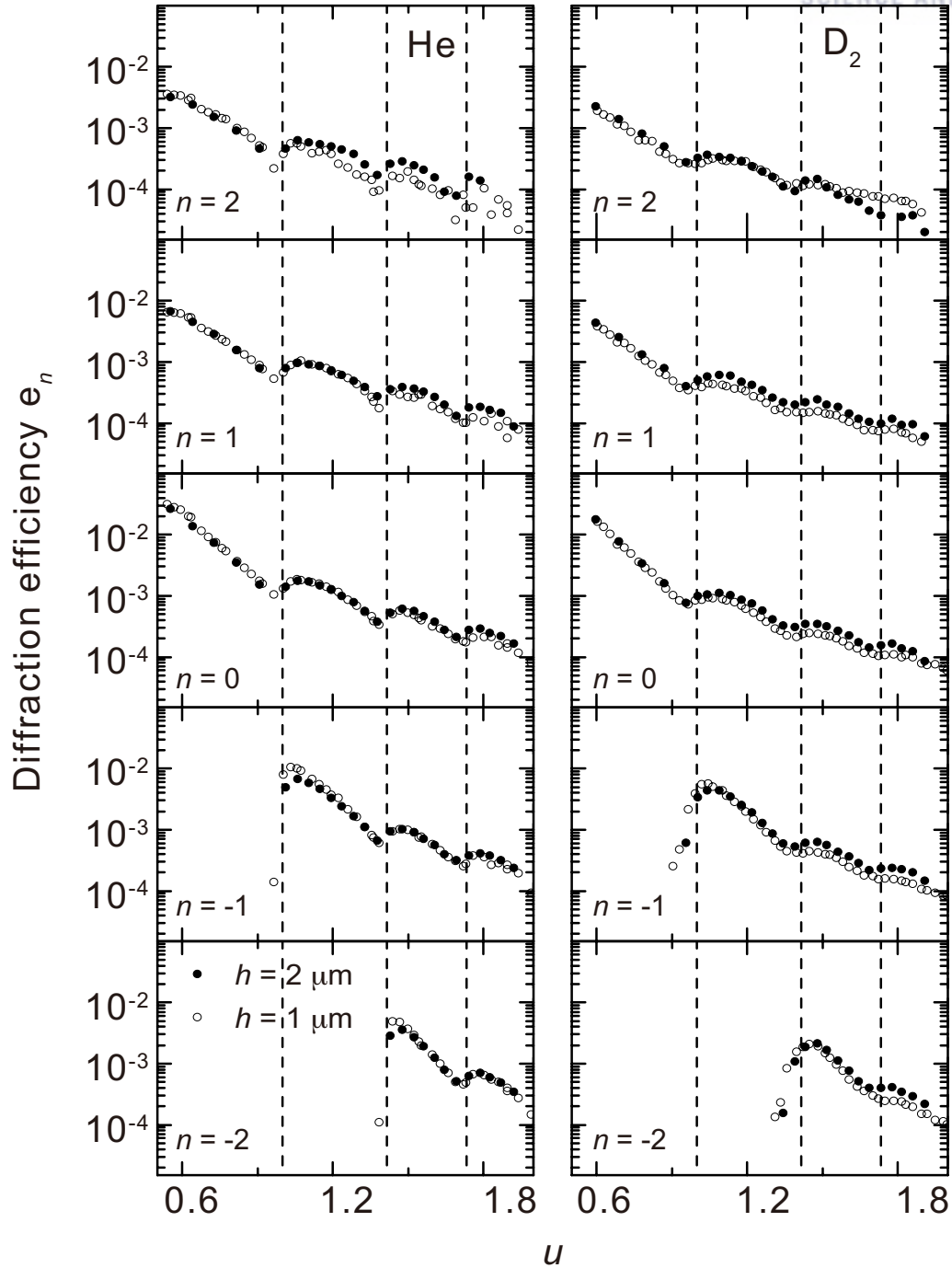
Figure 4.3: Diffraction efficiencies e_n of He (left column) and D_2 (right column) as a function of u measured from two square wave gratings which have the same period $d = 400\ \mu$m and strip width 10 μm at source temperature of 51.8 K (corresponding de Broglie wavelength $\lambda = 136$ pm) on a logarithmic scale. Open black circles (full black circles) represent the experimental results obtained from the grating whose structural height is 1 μm (2 μm).

4.2.2   Different Grating Periods
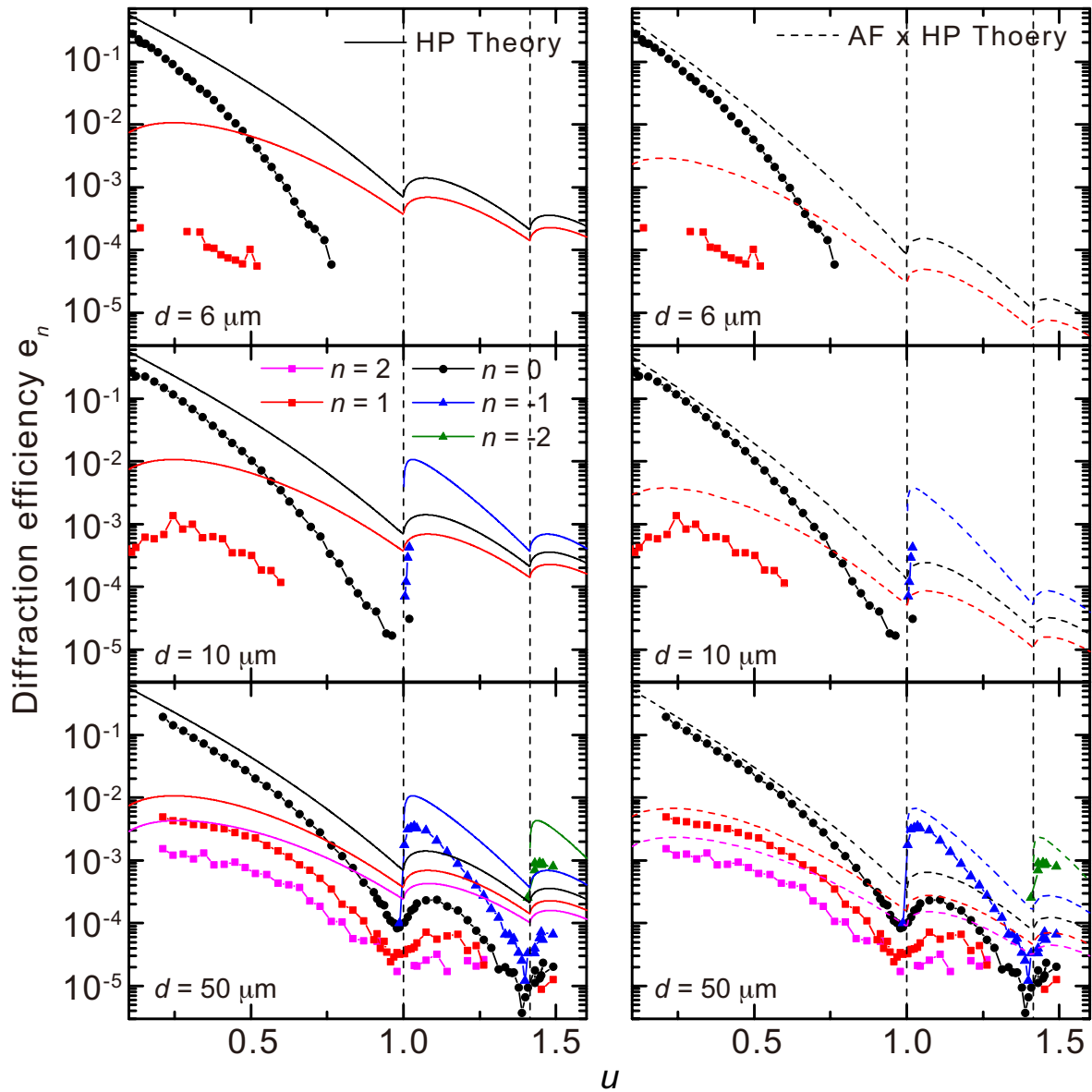
Figure 4.4: Diffraction efficiencies e_n of He as a function of u from square wave gratings of 6 μm (first row), 10 μm (second row), and 50 μm (third row) periods with 2 μm strip width at source temperature of 51.8 K (corresponding de Broglie wavelength $\lambda = 136$ pm) on a logarithmic scale. Colored solid lines in the figures on the left column show the theoretical diffraction efficiencies calculated for the ideal half-plane model while colored dashed lines on the right column show theoretically calculated attenuated efficiencies.

Diffraction efficiencies of He from the square wave gratings of 6, 10, and 50 μm periods with 2 μm strip width along with the HP theory lines (left column) and theoretically calculated attenuated efficiencies (right column) are presented in Fig. 4.4. The positive-order-diffraction efficiencies are measured until the signal to noise of the diffracted peaks become less than 2 to minimize the fitting error. Here, we find that the diffracted peaks emerged from a shorter

period exhibit higher fitting error, attributing this to the surface defects arising from the fabrication process. In practice, defects are more likely to be found at the gratings with shorter periods or narrower strip widths under the photolithography technique. Since the non-specular efficiencies are not clear for the gratings of 6 μm and 10 μm periods, only specular efficiencies are compared to the theoretical results in Figure 4.5 to examine the tendencies of the attenuation effects for different grating periods.
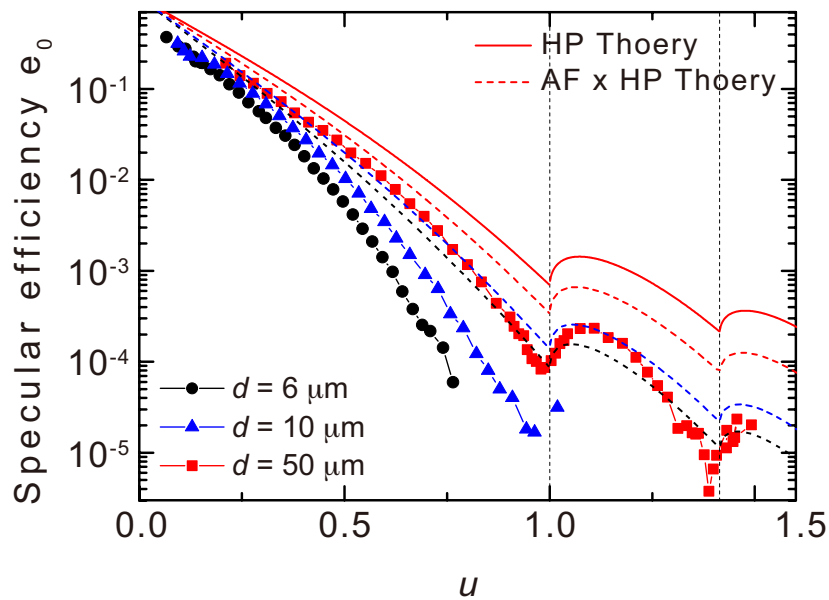
Figure 4.5: Specular efficiencies for the same experimental results shown in Fig. 4.4. The calculated attenuated specular efficiencies are presented with colored dashed lines while HP theory line is marked with a solid red line.

Overall, the experimental results are in better agreement with the attenuated efficiencies (right column) than the HP lines (left column) as shown in Fig. 4.4. Furthermore, not only a general tendency of measured specular efficiencies, i.e., higher efficiencies are shown from gratings with longer periods, but also relative gaps between measured specular efficiencies are explained better by considering the attenuation factors as presented in Fig. 4.5. However, as u increases, the theoretically obtained attenuated efficiencies gradually deviate from the observed efficiencies, overestimating the experimental results. Thus, the current theory for the attenuated efficiencies only gives us a qualitative picture.

Nonetheless, we get a hint for limitations on the current theory from our observation: deviations between the experimental results and the theoretical results begin at smaller values of u for shorter periods, implying that theoretical description of the attenuation factors is more appropriate for longer grating periods. In the theory of attenuation effects, the multiple scatterings of the phase-shifted waves induced by the particle-surface interactions are assumed to be negligible so the attenuation effect is not taken into account for the Fresnel integral. In other

words, this theory may not be appropriate to describe the attenuation effects as long as the multiple scattering takes place. Since multiple scatterings are more likely to occur at the gratings with shorter periods, such speculation is consistent with our observation.
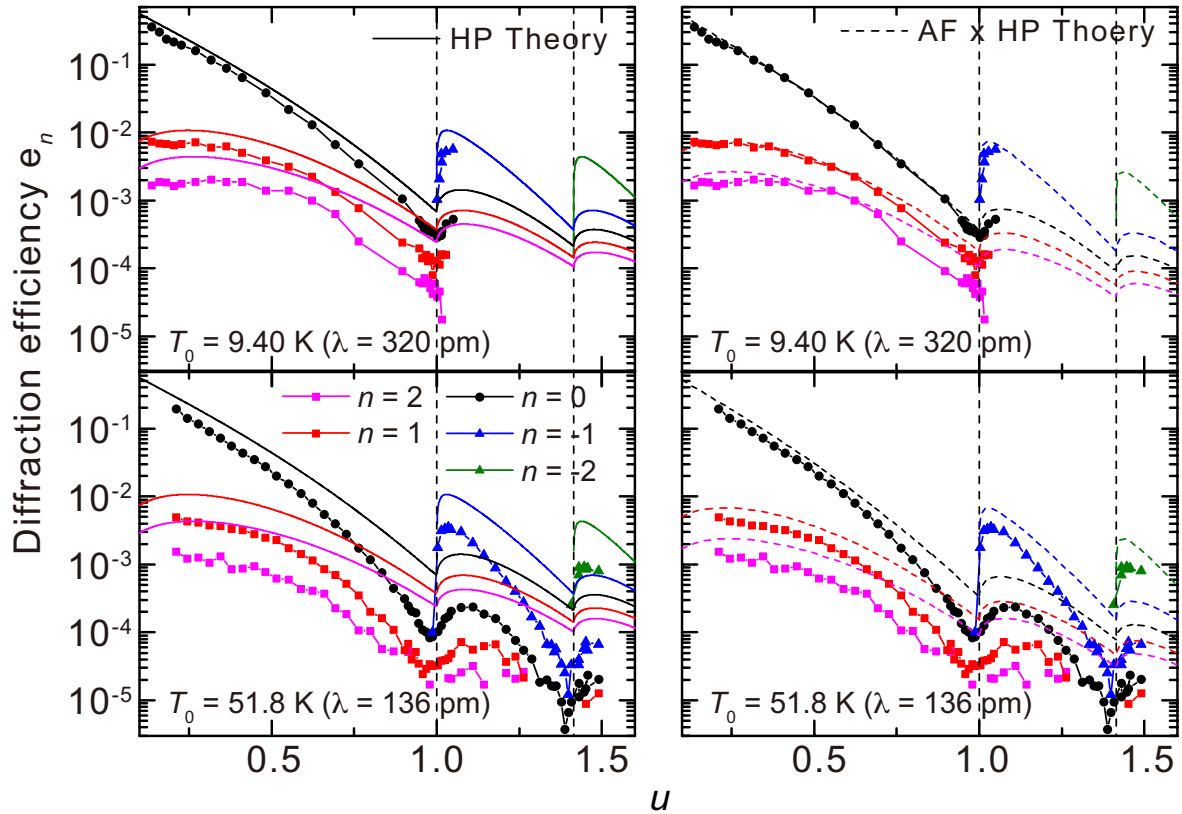
4.2.3 Different de Broglie Wavelengths

Figure 4.6: Diffraction efficiencies e_n of He as a function of u from the same square wave grating of 50 μm period with 2 μm strip width at source temperature of 9.40 K ($\lambda = 320$ pm, top) and 51.8 K ($\lambda = 136$ pm, bottom) on a logarithmic scale. Colored solid lines in graphs on the left column show the theoretical diffraction efficiencies calculated for the ideal half-plane model and the colored dashed lines on the right column show theoretically calculated attenuated efficiencies.

Diffraction efficiencies of He from the same square wave grating of 50 μm period and 2 μm strip width are measured at two different source conditions, 9.40 K ($\lambda = 320$ pm) and 51.8 K ($\lambda = 136$ pm). The experimental results along with the HP theory lines (left column) and theoretically calculated attenuated efficiencies (right column) are presented in Fig. 4.6. One of the experimental results which is measured at 51.8 K is presented once again to study the different attenuation effects for different wavelengths. Additionally, specular efficiencies of He measured at each condition are shown in Fig. 4.7 with the corresponding attenuated efficiencies and original HP theory line for the sake of comparison.

Here, as elsewhere in this subsection, theoretically calculated attenuated efficiencies not only show a better agreement with the experimental results (see Fig. 4.6) but also illustrate the general tendency of the attenuation effects for each case (see Fig. 4.7), providing a qualitative analysis on the different attenuation effects induced by the difference of de Broglie wavelengths. Meanwhile, it is noteworthy that the calculated attenuated efficiencies are almost

perfectly matched with the experimental results for the larger de Broglie wavelength while overestimating the experimental results obtained with the shorter de Broglie wavelength. Because multiple scatterings are more likely to occur for shorter wavelengths, those results further support our hypothesis as mentioned above: considering multiple scatterings of phase-shifted waves is a key for improving the current theory for the attenuation effect.
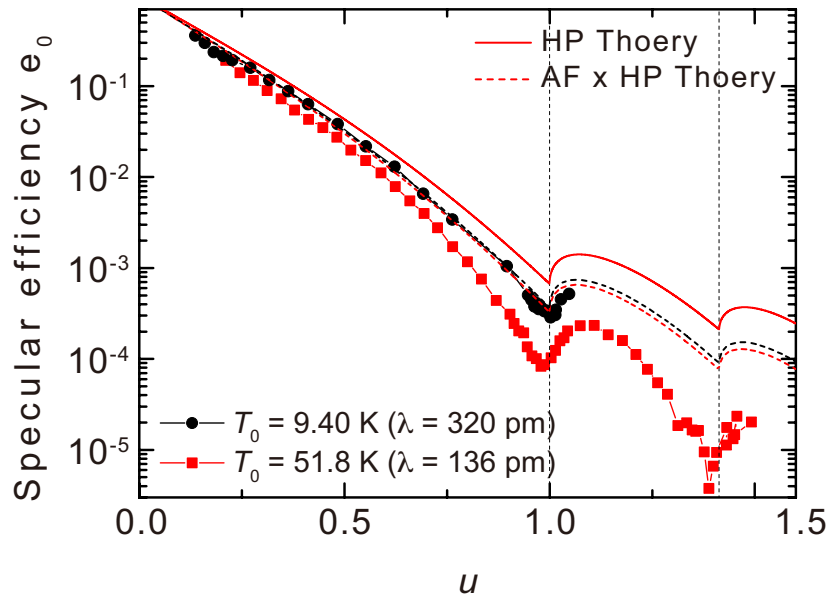

Figure 4.7: Specular efficiencies for the same experimental results in Fig. 4.6. The calculated attenuated specular efficiencies are presented with dashed lines while HP theory line is marked with a red solid line.

4.3 Possibility of Applying Half-Plane Reflection/Diffraction to Molecules

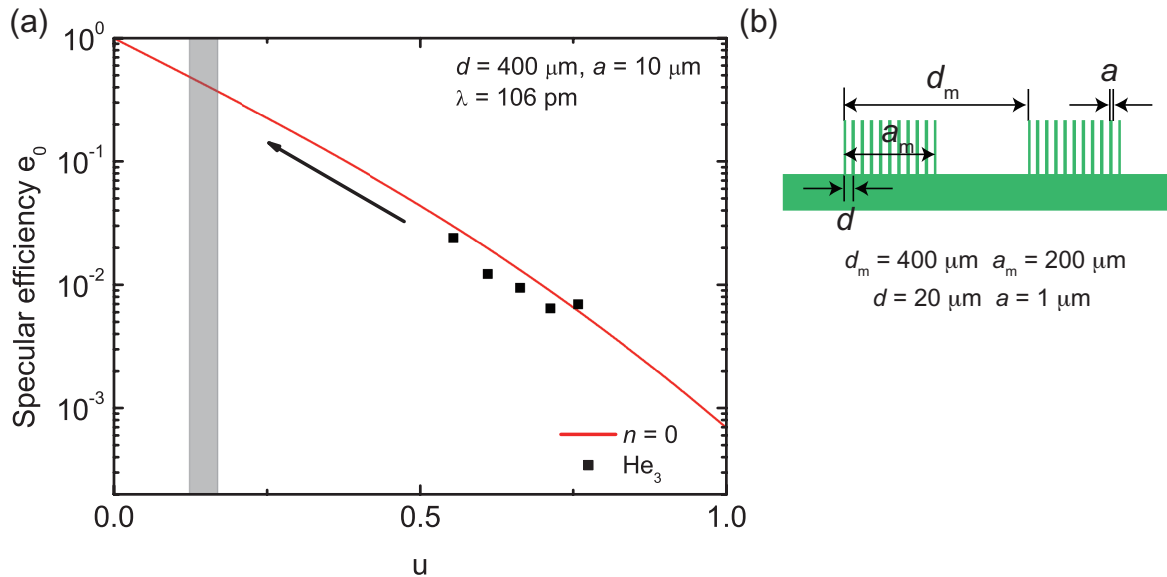### 4.3.1 Half-Plane Reflection/Diffraction of van der Waals Clusters

Figure 4.8: This image is taken from our previous paper (*89*). (**a**) Specular efficiency of He_3 from a square wave grating of 400 μm period and 10 μm strip width at source temperature of 9.40 K (corresponding wavelength $\lambda = 106$ pm). A solid red line shows a HP theory line for $n = 0$. (**b**) Sketch of a meta grating formed by identical patches (period $d_{\rm m}$, width $a_{\rm m}$) of half-plane array. This structure is expected to allow for efficient reflection and diffraction of fragile van der Waals clusters.

In the preceding section, we study non-negligible influences of particle-surface interactions on half-plane reflection/diffraction. Even so, the origin of ideal half-plane reflection/diffraction is nothing to do with van der Waals interactions, implying half-plane reflection/diffraction is expected to apply for fragile van der Waals clusters. The specular efficiency of helium trimer from a square wave grating of 400 μm period and 10 μm strip width was demonstrated in our previous paper (*89*) and is reproduced in Fig. 4.8 to suggest a new type of grating to study diffraction of fragile van der Waals clusters.

According to the theoretical description on half-plane reflection/diffraction (Section 2.2), specular efficiency rapidly increases while diffraction efficiencies are suppressed to 0 in the limit of $u \to 0$. As the scalable parameter u is proportional to the square root of the grating period d, higher specular efficiencies can be achieved by reducing grating periods. To effectively see this, a range of u which is achievable by using a shorter grating period of 20 μm is depicted by the gray shaded as shown in Fig. 4.8(a). In this regime of u, a specular efficiency of about 40 % is available, indicating a possibility of further applications. We can thus observe reasonably high reflection efficiencies by exploiting half-plane reflection/diffraction, yet diffraction efficiencies are still low to be measured for van der Waals clusters.

To overcome such a limitation, we suggest a new type of grating by designing a super-

periodic half-plane array. Figure 4.8(b) depicts a meta grating which are composed of both a small half-plane period d and a large grating super-period d_m. The combination of half-plane array and super-period grating will lead to diffraction at enhanced reflection probabilities as compared to previous experiments, opening up a possibility to study diffraction of fragile van der Waals clusters such as He_2 and He_3.

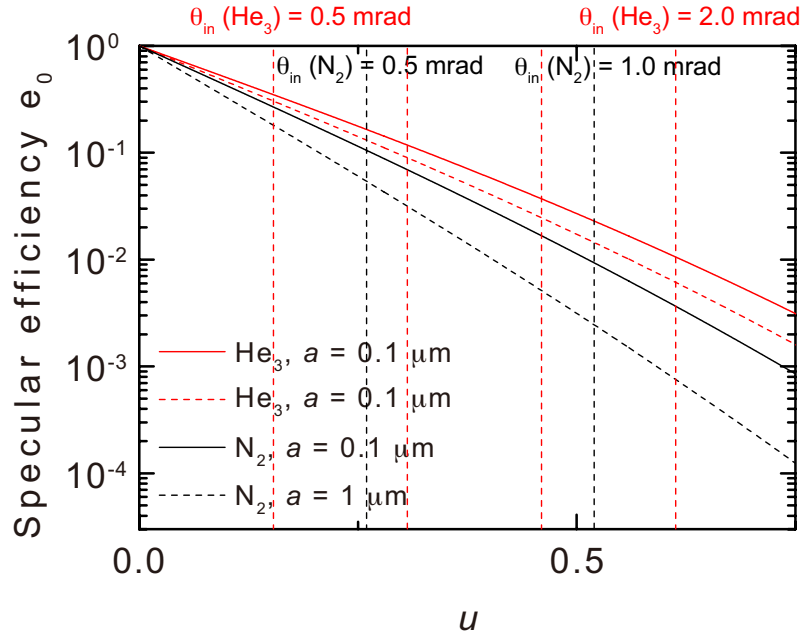### 4.3.2 Theoretical Analysis for Helium Trimer and Nitrogen

Figure 4.9: Theoretically obtained attenuated specular efficiencies of He_3 ($\lambda = 106$ pm) and N_2 ($\lambda = 37.0$ pm) measured from the square wave gratings of 20 μm period with 1 μm and 0.1 μm strip widths as a function of u. A solid red line (solid black line) represents the attenuated specular efficiency for the 0.1 μm strip width while a dashed red line (dashed black line) shows the attenuated specular efficiency for the 1 μm strip width for He_3 (N_2). Dashed vertical lines indicate the positions where corresponding incidence angles are 0.5, 1.0, 1.5, and 2.0 mrad.

We perform a theoretical study of matter-wave reflection optical phenomena from square-wave gratings of 20 μm period with 0.1 and 1 μm strip widths using He_3 and N_2 to see the applicability of half-plane reflection/diffraction to more general gases. Considering the boiling point of the nitrogen (77.4 K), the source temperature is assumed to be 100 K (corresponding de Broglie wavelength is 37.0 pm), while the source temperature is set at 9.40 K for He_3 (corresponding de Broglie wavelength is 160 pm).

Now that we know attenuation effects play an important role in matter-wave diffraction from square wave gratings, attenuated specular efficiencies of He_3 and N_2 rather than ideal HP theory lines are shown with corresponding incidence angles at intervals of 0.5 mrad (marked with dashed vertical lines) in Fig. 4.9. Considering the difference in polarizability, the van der Waals constant for nitrogen is assumed to be 10 times larger than helium, namely $C_3 = 2.0 \times 10^{-49}$ Jm^3. As nitrogen has higher polarizability than helium trimer, the attenuated specular efficiencies of N_2 are lower than those for He_3 as depicted in Fig. 4.9. Although overall specular efficiencies are rapidly decreased with increasing u, their efficiencies for both strip widths at an incidence angle of 0.5 mrad are still higher than 4%. Such a striking result is only available with half-plane reflection/diffraction. Reflectivity of nitrogen under quantum reflection, for instance, is already below 10^{-4} under the same condition of the source condition and

the incidence angle. Half-plane reflection/diffraction can thus be a powerful tool to extend the study of matter-wave optical phenomena to bigger molecules.

5   Conclusion

Within this work, matter-wave optical phenomena from periodically structured surfaces, a model system to study half-plane reflection/diffraction (HP), have been investigated using square wave gratings. By adopting a well-established HP theory performed by Bogomolny and Schmitz (*81*), quantitative comparison between theory and experiment have been available. In our previous work, we found that matter-wave reflection/diffraction for He deviates from the theoretical results of half-plane reflection/diffraction as strip widths of square wave gratings get larger, attributing this to a influence of quantum reflection (*89*). By carrying out similar studies for D_2, different propensities of matter-wave reflection/diffraction for different particles are presented: overall diffraction efficiencies are higher for He than D_2 under the same condition due to its higher probability of quantum reflection. Thus, we find that such difference of optical phenomena for different particles under the same condition results from the different interplay between quantum reflection and half-plane reflection/diffraction. On the other hand, we find that particle-surface interactions give rise to a reduction of half-plane reflection/diffraction efficiencies rather than a manifestation of quantum reflection for shorter strip widths. In order to effectively study the attenuated reflection/diffraction, theoretical analysis on attenuation effects obtained by Kouznetsov and Oberst (*69*) is adapted. Different attenuation effects thereby have been studied in three different conditions – different particles, different grating periods, and different de Broglie wavelengths. Overall, experimental results show a better agreement with theoretically calculated attenuated efficiencies than ideal half-plane reflection/diffraction theory lines, indicating the attenuation effects should be taken into account when dealing with half-plane reflection/diffraction for matter-waves. Nonetheless, the current theory of attenuation effects can provide us only qualitative analysis, implying that the theory needs to be improved for quantitative analysis. By comparing experimental results to the corresponding theoretical results of attenuated efficiencies at each condition, general tendencies are found: the theoretical description of the attenuation effects is more appropriate for longer grating periods and for shorter de Broglie wavelengths. This indicates that one of assumptions made in Kouznetsov and Oberst' theoretical description – multiple scatterings of phase-shifted waves are too weak to affect Fresnel integral, is not suitable for some conditions. We hereby suggest that a next step for improving the current theory is dealing with the multiple scatterings of phase-shifted waves. Furthermore, the studies on half-plane reflection/diffraction for fragile van der Waals clusters and bigger molecules have been carried out. By reproducing one of our previous results – reflection of He_3 from a square-wave grating was demonstrated – we show that the reflectivity of van der Waals clusters can be high enough to be measured under half-plane reflection/diffraction. However, studies on diffractions of van der Waals clusters remain to be difficult due to their low efficiencies. Here, we suggest a new type of grating by

combining two different grating periods. Such super-periodic half-plane array will enable us to observe enhanced diffraction efficiencies. In addition to that, theoretical study has been performed for attenuated efficiencies of nitrogen and helium trimer from square wave gratings of 20 μm period with 0.1 and 1 μm strip widths. We find that probability of half-plane reflection exhibit much higher than quantum reflection probability under the same condition, showing the applicability to general molecules.

References

1. J. Kuo, *Electron microscopy: methods and protocols* (Springer Science & Business Media, 2007), vol. 369.

2. P. J. Goodhew, J. Humphreys, R. Beanland, *Electron microscopy and analysis* (CRC Press, 2014).

3. E. Bauer, *Rep. Prog. Phys* **57**, 895 (1994).

4. N. De Jonge, F. M. Ross, *Nat. Nanotechnol.* **6**, 695 (2011).

5. C. J. Tandler, C. M. Libanati, C. A. Sanchis, *J. Cell. Biol.* **45**, 355 (1970).

6. S. D. Eder *et al.*, *Phys. Rev. A* **91**, 43608 (2015).

7. D. A. MacLaren, B. Holst, D. J. Riley, W. Allison, *Surf. Rev. Lett.* **10**, 249 (2003).

8. P. Witham, E. Sánchez, *Rev. Sci. Instrum.* **82** (2011).

9. T. Reisinger, B. Holst, *J. Vac. Sci. Technol. B* **26**, 2374 (2008).

10. M. Koch *et al.*, *Jour. Microsc.* **229**, 1 (2008).

11. T. Reisinger, S. Eder, M. M. Greve, H. I. Smith, B. Holst, *Microelectron. Eng.* **87**, 1011 (2010).

12. S. D. Eder, T. Reisinger, M. M. Greve, G. Bracco, B. Holst, *New J. Phys.* **14**, 073014 (2012).

13. A. Fahy, M. Barr, J. Martens, P. C. Dastoor, *Rev. Sci. Instrum.* **86**, 23704 (2015).

14. H. C. Schewe, B. S. Zhao, G. Meijer, W. Schöllkopf, *New J. Phys.* **11**, 113030 (2009).

15. I. Estermann, O. Stern, *Zeitschrift für Phys.* **61**, 95 (1930).

16. H. Friedburg, *Z. Phys.* **130**, 493 (1951).

17. W. H. Zinn, *Phys. Rev.* **71**, 752 (1947).

18. H. D. J., B. M. T., *Phys. Rev.* **81**, 498 (1951).

19. C. G. Shull, *Phys. Rev.* **179**, 752 (1969).

20. C. J. D. Germer, L. H.Germer, *Proc. N. A. S* **14**, 317 (1928).

21. P. H. Cutler, J. C. Davis, *Surf. Sci.* **1**, 194 (1964).

22. C. Adams, M. Sigel, J. Mlynek, *Phys. Rep.* **240**, 143 (1994).

23. J. B. Anderson, R. P. Andres, J. B. Fenn, *Adv. Chem. Phys. Mol. Beams* **10**, 275 (1966).

24. A. Libson *et al.*, *New J. Phys.* **8**, 77 (2006).

25. M. F. De Kieviet, D. Bahatt, G. Scoles, G. Vidali, M. Karimi, *Surf. Sci.* **365**, 789 (1996).

26. B. F. Mason, R. Williams, *Surf. Sci.* **45**, 141 (1974).

27. P. Zeppenfeld, K. Kern, R. David, U. Becher, G. Comsa, *Surf. Sci.* **285**, 461 (1993).

28. W. Sachtler, P. Van Der Plank, *Surf. Sci.* **18**, 62 (1969).

29. F. Traeger, H. Weiss, J. G. Skofronick, J. P. Toennies, *Phys. Rev. B* **67**, 035413 (2003).

30. M. F. Bertino, F. Hofmann, J. P. Toennies, *J. Chem. Phys.* **106**, 4327 (1996).

31. G. Benedek *et al.*, *Helium Atom Scattering from Surfaces*, vol. 27.

32. P. E. Moskowitz, P. L. Gould, S. R. Atlas, D. E. Pritchard, *Phys. Rev. Lett.* **51**, 370 (1983).

33. P. E. Moskowitz, P. L. Gould, D. E. Pritchard, *J. Opt. Soc. Am. B* **2**, 1784 (1985).

34. P. J. Martin, B. G. Oldaker, A. H. Miklich, D. E. Pritchard, *Phys. Rev. Lett.* **34**, 343 (1988).

35. P. J. Martin, P. L. Gould, B. G. Oldaker, A. H. Miklich, D. E. Pritchard, *Phys. Rev. A* **36**, 2495 (1987).

36. V. I. Balykin, V. S. Letokhov, Y. Ovchinnikov, A. I. Sidorov, *Reflection of an atomic beam from a gradient of an optical field*, 1987.

37. V. I. Balykin, V. S. Letokhov, Y. B. Ovchinnikov, A. I. Sidorov, *Phys. Rev. Lett.* **60**, 2137 (1988).

38. D. W. Keith, M. L. Schattenburg, H. I. Smith, D. E. Pritchard, *Phys. Rev. Lett.* **61**, 1580 (1988).

39. W. Schöllkopf, J. P. Toennies, *Science* **266**, 1345 (1994).

40. R. E. Grisenti, W. Schöllkopf, J. P. Toennies, G. Hegerfeldt, T. Köhler, *Phys. Rev. Lett.* **83**, 1755 (1999).

41. R. B. Doak *et al.*, *Phys. Rev. Lett.* **83**, 4229 (1999).

42. O. Carnal, M. Sigel, T. Sleator, H. Takuma, J. Mlynek, *Phys. Rev. Lett.* **67**, 3231 (1991).

43. S. Gerlich *et al.*, *Nat. Phys.* **3**, 711 (2007).

44. M. Berninger, A. Stefanov, S. Deachapunya, M. Arndt, *Phys. Rev. A* **76**, 013607 (2007).

45. M. D. Gregoire, I. Hromada, W. F. Holmgren, R. Trubko, A. D. Cronin, *Phys. Rev. A* **92**, 052513 (2015).

46. M. A. Kasevich, D. S. Weiss, S. Chu, *Opt. Lett.* **15**, 607 (1990).

47. A. Landragin *et al.*, *Europhys. Lett.* **39**, 485 (1997).

48. D. Meschede, F. Lison, R. Wynands, W. G. Kaenders, A. Richter, *Nature* **375**, 214 (1995).

49. D. C. Lau *et al.*, *J. Opt. B Quantum Semiclassical Opt.* **1**, 371 (1999).

50. R. E. Grisenti *et al.*, *Phys. Rev. A* **61**, 033608 (2002).

51. A. M. Lahee, J. R. Manson, J. P. Toennies, C. Wöll, *Phys. Rev. Lett.* **57**, 471 (1986).

52. J. Leigh, *J. Phys. C* **4**, L359 (1971).

53. W. H. Weinberg, *J. Phys. C Solid State Phys.* **5**, 2098 (1972).

54. S. V. Krishnaswamy, D. R. Frankl, G. Derry, D. Wesner, *Surf. Sci.* **77**, 493 (1978).

55. C. Henkel, C. I. Westbrook, A. Aspect, *J. Opt. Soc. Am. B* **13**, 233 (1996).

56. W. Brenig, *Z. Phys. B* **36**, 227 (1979).

57. E. R. Bittner, *J. Chem. Phys.* **100**, 5314 (1994).

58. D. P. Clougherty, W. Kohn, *Phys. Rev. B* **46**, 4921 (1992).

59. T. W. Hijmans, J. T. Walraven, G. V. Shlyapnikov, *Phys. Rev. B* **45**, 2561 (1992).

60. A. Mody, M. Haggerty, J. M. Doyle, E. J. Heller, *Phys. Rev. B* **64**, 085418 (2001).

61. S. Miret-Artés, E. Pollak, *J. Phys. Chem. Lett.* **8**, 1009 (2017).

62. B. S. Zhao, G. Meijer, W. Schöllkopf, *Science* **331**, 892 (2011).

63. R. B. Doak, A. V. G. Chizmeshya, *Europhys. Lett.* **51**, 381 (2000).

64. H. Friedrich, G. Jacoby, C. G. Meister, *Phys. Rev. A* **65**, 032902 (2002).

65. J. Petersen, E. Pollak, S. Miret-Artes, *Phys. Rev. A* **97**, 042102 (2018).

66. F. Shimizu, *Phys. Rev. Lett.* **86**, 987 (2001).

67. T. A. Pasquini *et al.*, *Phys. Rev. Lett.* **93**, 223201 (2004).

68. H. Oberst, Y. Tashiro, K. Shimizu, F. Shimizu, *Phys. Rev. A* **71**, 052901 (2005).

69. D. Kouznetsov, H. Oberst, *Phys. Rev. A* **72**, 013617 (2005).

70. H. Oberst, D. Kouznetsov, K. Shimizu, J. I. Fujita, F. Shimizu, *Phys. Rev. Lett.* **94**, 013203 (2005).

71. F. Shimizu, J. I. Fujita, *J. Phys. Soc. Japan* **71**, 5 (2002).

72. V. Druzhinina, M. DeKieviet, *Phys. Rev. Lett.* **91**, 193202 (2003).

73. B. S. Zhao, H. C. Schewe, G. Meijer, W. Schöllkopf, *Phys. Rev. Lett.* **105**, 133203 (2010).

74. B. S. Zhao, S. A. Schulz, S. A. Meek, G. Meijer, W. Schöllkopf, *Phys. Rev. A* **78**, 010902 (2008).

75. B. S. Zhao, G. Meijer, W. Schöllkopf, *Phys. Rev. Lett.* **104**, 240404 (2010).

76. B. S. Zhao, G. Meijer, W. Schöllkopf, *New J. Phys.* **13**, 065017 (2011).

77. J. F. Carlson, A. E. Heins, *Q. Appl. Math.* **4**, 313 (1947).

78. A. Heins, J. F. Carlson, *Q. Appl. Math.* **5**, 281 (1947).

79. B. A. Lengyel, *J. Appl. Phys.* **22**, 265 (1951).

80. J. J. Brady, M. D. Pearson, S. R. Peoples, *J. Appl. Phys.* **23**, 964 (1952).

81. E. Bogomolny, C. Schmit, *Nonlinearity* **16**, 2035 (2003).

82. M. Born, E. Wolf, *Principles of optics: electromagnetic theory of propagation, interference and diffraction of light* (Elsevier, 2013).

83. P. J. Richens, M. V. Berry, *Physica D.* **2**, 495 (1981).

84. E. Bogomolny, C. Schmit, *Phys. Rev. Lett.* **92**, 244102 (2004).

85. E. Bogomolny *et al.*, *Phys. Rev. Lett.* **97**, 254102 (2006).

86. L. E. Vogler, *Radio Sci.* **17**, 1541 (1982).

87. J. Walfisch, H. Bertoni, *IEEE Trans. Antennas Propag.* **36**, 1788 (1988).

88. H. L. Bertoni, *IEEE Trans. Antennas Propag.* **40**, 170 (1992).

89. J. H. Lee *et al.*, *Phys. Rev. Lett.* **122**, 40401 (2019).

90. W. Schöllkopf, J. P. Toennies, *J. Chem. Phys.* **104**, 1155 (1996).

91. W. Zhang *et al.*, *ChemPhysChem* **17**, 3670 (2016).

Appendix A

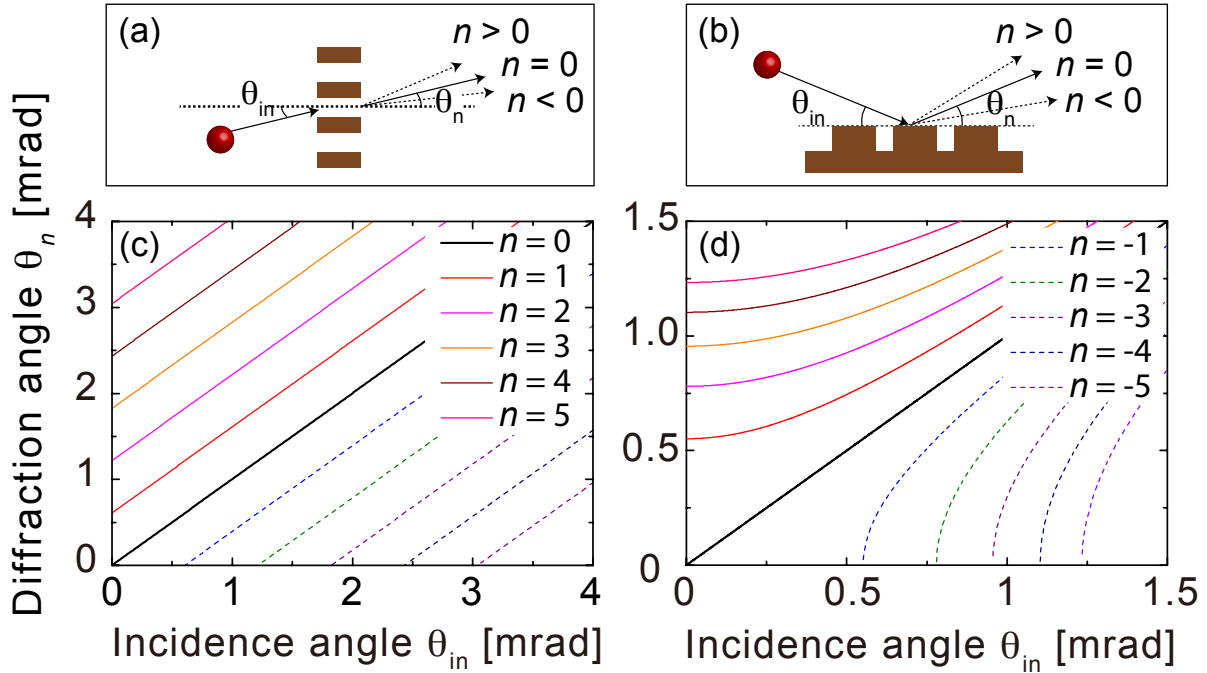## Nano-Fabricated Transmission Grating vs. Micro-Fabricated Reflection Grating

Figure A.1: Schematics of wave-scattering from (**a**) the nano-transmission grating whose period is 100 nm and (**b**) the square-wave grating whose period is 400 μm. Calculated angular positions of the n-th order diffraction angles versus incidence angle θ_{in} of the matter-wave whose de Broglie wavelength is 136 pm over certain ranges of incidence angles from each grating are shown in (**c**) and (**d**), respectively. Dashed lines(solid lines) indicate the diffraction angles of negative orders (positive and specular orders).

Under the grazing incidence condition, resolved diffraction peaks have been observed from micro-fabricated reflection-gratings (*74, 75, 89, 91*). Figure A.1(a) and A.1(b) show the schematics of matter-wave scattering from a transmission grating with the period of 100 nm and a square-wave grating whose period is 400 μm, respectively. For the sake of convenience, the incidence angle θ_{in} and the diffraction angle θ_n are defined with respect to the normal line for the nano-transmission grating while those are determined from the grating-surface plane for the square-wave grating. A sign of the diffraction order is defined in a way that diffraction angles of positive orders are larger than those of negative orders. In order to observe the difference between two gratings, n-th-order diffraction angles over certain ranges of incidence angles from each grating are calculated by the grating equation in Fig. A.1(c) and A.1(d), respectively. Here, matter-wave de Broglie wavelength is fixed at 136 pm. Assuming the angular resolution of the atomic beam is around 100 μrad, up to 5th order diffraction peaks can be observed at grazing incidence angles from the micro-fabricated reflection-grating as it can be

from a nano-transmission grating at a normal incidence condition. Considering the fact that the reflection and diffraction efficiencies are increased as incidence angle goes smaller from the reflection-type grating, diffraction efficiencies from square-wave gratings are expected to be higher as much as those efficiencies from transmission grating. Therefore, micro-fabricated structures can act as a matter-wave-grating and it appears important for the generality of matter-wave elements due to its lower price and size-limit than nano-fabricated structures like the nano-transmission grating. Thus, micro-fabricated solid structures can be a good candidate for practical matter-wave optical instruments as exploiting grazing incidence condition.

Appendix B

Position Optimization of a Mirror

The relative position of a mirror in the beam path is crucial to evaluate an approximate value of blocked direct beams because they can not be measured directly from the experiment. When the mirror is positioned at the center of the beam path, the amounts of the cut beam (wing) and blocked beam are the same, i.e., the amount of the blocked beam can be estimated as that of the cut beam. Hence, the procedure of optimizing the mirror's position utilized in our work is presented here.
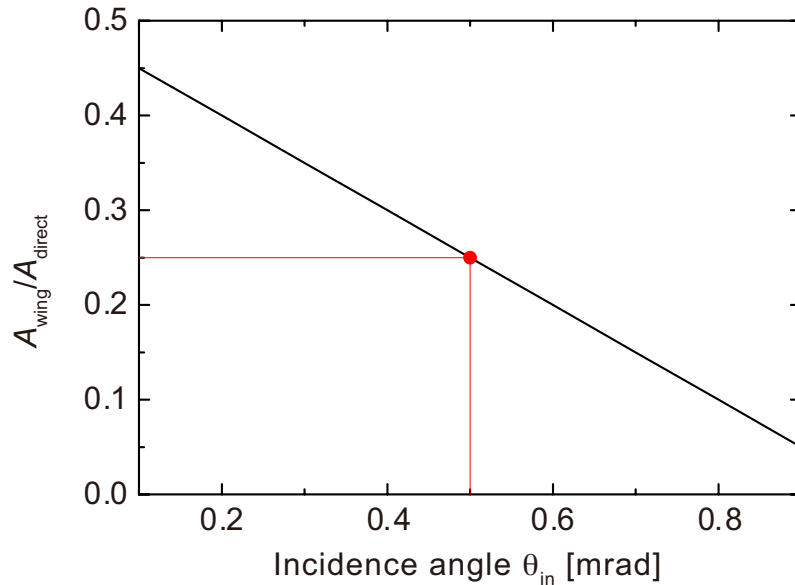

Figure B.1: A ratio of the area of the wing to the area of the direct beam as a function of a incidence angle θ_{in}. The ratio corresponding to the incidence angle of 0.5 mrad is denoted as a red dot

Here, the dimeter of the incident beam arriving at the grating is assumed to be around $50~\mu$m for the quantitative analysis on the incident beam really taking part in the scattering process. When the mirror is mounted at the center of the beam path while forming an incidence angle θ_{in}, the diameter of the incident beam is estimated as $50~\sin\theta_{\text{in}} \approx 50~\theta_{\text{in}}$ mm, i.e., a ratio of the wing to the direct beam is estimated as following relation:

$$\frac{A_{wing}}{A_{direct}} = \frac{1}{2} \times \frac{50\theta_{\text{in}}}{50} = \frac{\theta_{\text{in}}}{2}. \tag{5.2}$$

Figure B.1 shows the ratio as a function of the incidence angle θ_{in}. As a reference value, we adjust the grating position at 0.5 mrad of the incidence angle θ_{in} until $\frac{A_{wing}}{A_{direct}} = 0.25$ as indicated with a red dot.

There are two motors to control a center-of-mass motion and a rotation of the mirror, de-
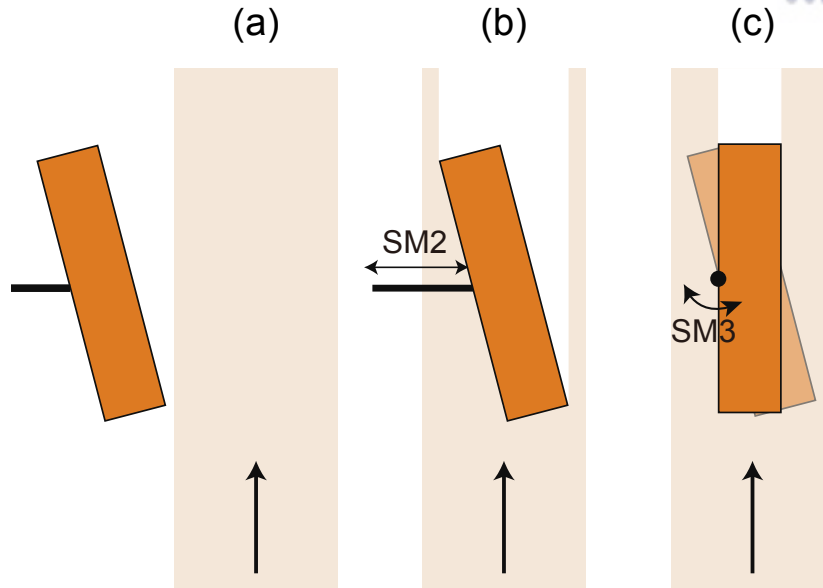
Figure B.2: Sketch of (a) step 1, (b) 3, and (c) 4 described in the main text (not to scale). The arrow displays the direction of the direct beam.

noted as SM2 (step motor 2) and SM3 (step motor 3) in our experiment as presented in Fig. B.2. Each motor is electronically controlled using a computer program developed with the software LabVIEW. With this, the incidence angle is finely adjusted whereby 0.048 mrad of angular resolution is achieved. The details of the optimization procedure are described below:

1. make sure that the mirror is totally pushed away from the beam path and rotated counterclockwise as depicted in Fig. B.2(a).

2. position the detector at the center position of the direct beam x_{direct}, thereby we can monitor the intensity of the direct beam.

3. push the mirror inside the beam path through adjusting SM2 until the signal starts to be decreased (see Fig. B.2(b)).

4. rotate the mirror clockwise by SM3 until the signal becomes to go down again (see Fig. B.2(c)).

5. measure an angular spectrum to investigate the incidence angle.

6. repeat the step 3 to 5 until the incidence angle reaches 0.5 mrad.

7. push the mirror through SM2 until the ratio of the area of the wing to that of the direct beam becomes a quarter.

Appendix C

Fabrication of Gratings

Each of the four reflection gratings used in this work consists of a 50-mm-long microstructured array of parallel strips made of 1-μm-thick photoresist patterned on a gold mirror. Figure 11 shows microscopy images of all gratings used in this work. The center-to-center distance of the strips defines a period d and 4-mm-long strips have widths a. Given this geometry, the gold surface between the strips is completely shadowed by the strips for all incidence angles used in this work.

The fabrication of the gratings was performed using conventional photolithography. Photoresist (AZ 5214E, AZ Electronic Materials) was spin-coated onto a commercial gold mirror (Thorlabs PFSQ20-03-M03) at 4000 r.p.m. The mirror was soft-baked at 105 °C for 90 s, followed by UV exposure through a photomask at 100 mJ/cm^2 (MA6, Suss MicroTec) and development (MIF 300, AZ Electronic Materials). The thickness of the grating strips was measured using a surface profiler (P6, KLA Tencor). We also prepared a flat sample formed by blank (not structured) photoresist of the same thickness (1 μm) making it possible to compare the reflectivity measured with the unstructured photoresist to the one measured with the gratings.

Acknowledgements

To conclude this thesis, I would like to express my gratitude to the many people who helped me in doing my research. First, I would like to thank my advisor, Bum Suk Zhao for giving me the opportunity to do this research in his group and for the guidance and the support on my master studies. I would also like to thank my group colleagues Byung Gwan Jin, Tae Woo Kim, and specially, Lee Yeong Kim for the partnership all these years.

I also thank my parents enough for their support and unconditional love: my father has been my mentor for the past 23 years and will be my inspiration in my life; my mother has always taken my side for everything. I also would like to thank my two sisters for being my forever friends. I love you all so much. 항상 나를 믿어주고 응원해주는 우리 가족, 너무 사랑하고 고마워요.

I can't forget to thank the colleagues at FHI (Fritz-Haber Institute, Berlin). I was fortunate to spend the most of my graduate study period in Germany. It was an honor for me to work with Wieland Schöllkopf. He not only helped me adapt to living in Germany, but also taught me the the details of the experimental apparatus. I also would like to thank Gerard Meijer for hosting the MAGIE laboratory at FHI. I am greatly in debt to 라윤언니 (Rayoon Chang), Mallikarjun Karra, and Bruno Credidio for being my best friend in Germany. I always miss you guys.